https://doi.org/10.1016/j.ijheatmasstransfer.2021.121786

Droplet evaporation and boiling for different mixing ratios of the silver-graphene hybrid nanofluid over heated surfaces

F.R. Siddiqui[1], C.Y. Tso[2], S.C. Fu[3], H.H. Qiu[1], Christopher Y. H. Chao[3*]

[1]Department of Mechanical and Aerospace Engineering, The Hong Kong University of Science and Technology, Hong Kong

[2]School of Energy and Environment, City University of Hong Kong, Hong Kong

[3]Department of Mechanical Engineering, The University of Hong Kong, Hong Kong

*Corresponding Author Tel.: +852 3917 2800

E-mail Address: cyhchao@hku.hk

Postal Address: Department of Mechanical Engineering, The University of Hong Kong, Pokfulam Road, Hong Kong

Abstract

Thermal management of many high heat flux devices depends on droplet based cooling, such as the spray cooling or electro-wetting for hotspot cooling. Recently, heat dissipation in these devices increased to unprecedented levels, pressing a need for advanced thermal fluids in droplet based cooling systems. In this paper, we address this challenge by investigating the evaporation and boiling performance of the silver-graphene hybrid nanofluid (SGHF) droplet for its various mixing ratios and droplet sizes on a heated copper and a residue surface, obtained from the evaporation of the first SGHF droplet. The results show that low mixing ratio (MR ≤ 0.1) SGHF droplets exhibit highest evaporation rates for substrate temperature (T_s) in a range of 25 °C ≤ T_s ≤ 100 °C. However, this trend is reversed in the nucleate boiling regime, where high mixing ratio (MR ≥ 0.9) droplets give highest evaporation rates. Moreover, all SGHF droplets, irrespective of their mixing ratio, exhibit similar evaporation rates in the film-boiling regime. Furthermore, the SGHF droplet evaporation rate on its porous residue surface increases up to 173% for 25°C ≤ T_s ≤ 100 °C and by an order of magnitude in the nucleate boiling regime as compared to a plain copper surface. We also show that besides the synergistic thermal effect, the thermal Marangoni convection also affects the SGHF droplet evaporation rate. Moreover, we develop a diffusion-convection evaporation model that can predict the evaporation rate for different mixing ratios of the SGHF

droplet on heated copper and residue surfaces. Moreover, we demonstrate that the latent heat flux up to 890 W/cm^2 and 850 W/cm^2 can be achieved using a SGHF droplet on heated copper and residue surfaces, respectively, suggesting its potential application in high heat flux device cooling. Finally, we discuss the effects of spray hydrodynamic parameters on critical heat flux of the SGHF spray cooling.

Keywords: Hybrid nanofluid; droplet residue; evaporation; boiling; Marangoni effect.

Nomenclature

A_c	Droplet-solid contact area, m^2	R	Droplet contact radius, m
Bo_d	Dynamic bond number	RH	Relative humidity
C	Molar concentration, mol.m^{-3}	$SGHF$	Silver-graphene hybrid nanofluid
C_p	Specific heat capacity, J.kg^{-1}.K^{-1}	T_a	Ambient temperature, °C
D	Mass diffusivity, m^2.s^{-1}	T_s	Surface temperature, °C
E	Net evaporation rate, µl.s^{-1}	T_o	Reference temperature, °C
E_D	Evaporation rate due to mass diffusion, µl.s^{-1}	t	Time, s
E_{MC}	Evaporation rate due to Marangoni convection, µl.s^{-1}	V_{fd}	Volume of the first droplet, µl
GNP	Graphene nanoplatelets	V_{sd}	Volume of the second droplet, µl
h_{fg}	Latent heat of vaporization, J.kg^{-1}	Vi	Initial droplet volume, µl
J_o	Evaporation constant	x_v	Vapor mole fraction
k	Thermal conductivity, W.m^{-1}.K^{-1}	***Greek Symbols***	
L_p	Leidenfrost point	α	Thermal diffusivity, m^2.s^{-1}
Ma	Marangoni number	β	Volumetric expansion coefficient, K^{-1}
MR	Mixing ratio	ϕ	Volume fraction
P_a	Ambient pressure, Pa	ρ	Density, kg.m^{-3}
P_{sat}	Saturation pressure, Pa	μ	Dynamic viscosity, Pa.s
Q	Latent heat flux, W.cm^{-2}	γ	Surface tension, N.m^{-1}
Ra	Rayleigh number		

1. Introduction

Droplet based cooling systems are widely used in thermal management of high heat flux devices due to several benefits, such as high heat transfer rates, low thermal contact resistance and large area to volume ratio, to name a few. However, with progressive demand for improved system performance and dense packaging, heat dissipation in these devices recently increased to alarming levels, resulting in pre-mature device failures. This halted further growth of these devices due to the limited cooling capacity of existing heat transfer fluids. This challenge can be addressed by using advanced thermal fluids with high heat transfer rates, such as nanofluids, in droplet based cooling systems.

Nanofluids exhibit much better thermal properties than conventional fluids (such as water) due to high thermal conductivity of suspended nanoparticles [1–4]. The thermal conductivity of nanofluids increases with increasing temperature and particle concentration [5–8]. However, as the particle concentration increases, the nanofluid viscosity also increases that results in high pressure drop and clogging issues in cooling applications [9–12]. Moreover, high nanoparticle concentration increases particle-particle interactions resulting in rapid agglomeration and sedimentation [13,14]. These issues make single particle nanofluids less favourable for thermal cooling applications [15]. Another limitation is that single particle nanofluids lack overall hydro-thermal characteristics, as some nanofluids are more stable but thermally less conductive (such as metal-oxide nanofluids), while others are less stable but thermally more conductive (such as metal based nanofluids) [16,17]. Considering these limitations for single particle nanofluids, researchers recently proposed the next generation of nanofluid and termed it ‘hybrid nanofluid’ [18–20].

The hybrid nanofluid comprises two different nanoparticle types and outperforms the single particle nanofluid due to its improved hydrothermal properties (enhanced stability and high thermal conductivity). A highly stable nanoparticle type (such as metal-oxide nanoparticles) when dispersed with a highly conductive nanoparticle type (such as metal nanoparticles) in a base fluid forms a hybrid nanofluid exhibiting better overall hydrothermal properties than single particle nanofluids [16]. Besides improved hydrothermal properties, hybrid nanofluids are also preferred over single particle nanofluids due to their synergistic thermal effects [21–23]. In single particle nanofluids, there exists thermal contact resistance among suspended nanoparticles. Adding another

nanoparticle type creates a thermal pathway that rapidly transports heat and reduces thermal contact resistance leading to synergistic thermal effects in hybrid nanofluids [24]. Due to synergistic thermal conductivity, hybrid nanofluids exhibit much better thermal properties than single particle nanofluids and can be used at low particle concentration in cooling applications [19,20,25–27]. The synergistic thermal conductivity and improved hydrothermal properties make hybrid nanofluids better candidates for droplet based cooling of high heat flux devices than single particle nanofluids.

Although hybrid nanofluids received much attention in recent past, the hybrid nanofluid based droplet evaporation on heated surfaces has not been investigated by research community. However, a few researchers reported the droplet evaporation of single particle nanofluids over heated surfaces. Sefiane and Bennacer [28] showed that droplet evaporation rate of single particle nanofluid and base fluid is almost the same for small droplet contact radius (< 0.7 mm) on a heated PTFE surface. However, the nanofluid droplet exhibits higher evaporation rate than base fluid droplet for large droplet contact radius on a heated surface. Kim [29] also reported higher evaporation rate for copper-oxide (CuO) nanofluid droplet as compared to water droplet on a heated copper surface. He suggested high thermal conductivity of CuO nanofluid as the main reason for its enhanced droplet evaporation rate. Al-Sharafi et al. [30] studied the internal flow in an evaporating CNT nanofluid droplet on a heated surface and showed that Marangoni forces have a predominant effect on droplet internal flow field as compared to buoyancy forces. However, in another research on an evaporating CNT nanofluid droplet over a heated hydrophobic surface, they concluded that both Marangoni and natural convection affect the droplet internal flow field [31].

While a few researchers reported the droplet boiling of single particle nanofluids, there is still no research to date on the hybrid nanofluid droplet boiling. Research suggests that single particle nanofluid droplets give higher heat flux and boiling heat transfer rates than their base fluid droplets [32–34]. Despite enhanced evaporation and boiling performance, as already discussed, single particle nanofluids are not suitable candidates for thermal cooling systems mainly due to their poor hydrothermal characteristics. Therefore, the evaporation and boiling performance of hybrid nanofluid droplets must be thoroughly investigated, as they are better alternatives to single particle nanofluids and may address heat dissipation issues in high heat flux devices.

In this research, several nanoparticle combinations were initially considered to obtain hybrid nanofluids exhibiting synergistic thermal conductivity, such as, Ag-GNP, Ag-CNT, Cu-Al_2O_3, Cu-GNP, Zn-CNT and Zn-GNP. Among all these combinations, only silver-graphene hybrid nanofluid (SGHF) exhibited synergistic thermal conductivity, as it depends on inter-particle compatibility, size and shape of dispersed nanoparticles in hybrid nanofluids [35]. Han et al. [24] used different nanoparticles (hybrid sphere and CNT) than that used in current study and reported the effective thermal conductivity enhancement by 21%, where they attributed these synergistic effects to thermal pathway between several CNT's attached to the hybrid sphere surface. Moreover, to our best knowledge, composite nanofluids with three or more different nanoparticles have not been investigated to date possibly due to more complexities and variables (such as high mixing ratio combinations) involved than single particle nanofluids or hybrid nanofluids.

Considering immense heat dissipation in high heat flux devices, the main aim of this study is to investigate the synergistic thermal potential of the silver-graphene hybrid nanofluid (SGHF) for droplet based cooling systems. Therefore, as a novelty of this research, we initially investigate the effect of SGHF mixing ratio on its synergistic thermal behaviour. Subsequently, we study effects of mixing ratio and droplet volume on the SGHF droplet evaporation performance in a sub-boiling regime and three distinct boiling regimes, i.e., nucleate boiling, transition boiling and film boiling. In this research, we investigate the SGHF droplet evaporation and boiling processes on two different heated surfaces, that is, a plain copper surface and a porous residue of different sizes, obtained from the evaporation of the first SGHF droplet. The main motivation of this research is to investigate the SGHF mixing ratio that gives the highest evaporation and boiling performance over plain copper and its respective residue surface. Another motivation is to investigate the residue size effect on evaporation and boiling performance of the subsequent SGHF droplet. This is because in any hybrid nanofluid droplet based cooling system (such as the spray cooling), droplet residues of different sizes may form on substrate (due to poly-disperse spray droplets or due to droplet coalesce or break-up before impaction on the substrate). Such residues of different sizes may have different effect on evaporation and boiling performance of subsequent hybrid nanofluid droplets. To test this hypothesis, we recently studied the residue size and wetting effects on evaporation performance of the subsequent hybrid nanofluid droplet [17,36]. However, these

studies were performed at room temperature for un-heated surfaces, where the residue effect was different from that observed in the current study for heated residue surfaces.

In this paper, besides synergistic thermal effect, we also investigate the droplet internal convection effects that may influence the SGHF droplet evaporation rate. Therefore, we develop a numerical model to understand thermal Marangoni and natural convection effects on internal flow field and temperature distribution within an evaporating SGHF droplet. Subsequently, we develop a diffusion-convection evaporation model that considers the combined effect of mass diffusion, synergistic thermal conductivity and droplet internal convection. Similar droplet evaporation models were also proposed by some other researchers [37,38]. However, their proposed models were based on single-phase droplets (without suspended solid particles), while our study involves suspended hybrid nanoparticles in SGHF droplets that give different evaporation rates than single-phase (water) droplets over heated surfaces, as further discussed in section 4 (Results and discussion). Moreover, the existing droplet evaporation models [37,38] do not consider the droplet internal effects due to suspended hybrid nanoparticles within the hybrid nanofluid droplet and therefore cannot be used in this study. Due to these limitations, we develop a new diffusion-convection evaporation model that incorporates the droplet surface effects (such as mass diffusion) as well as the droplet internal effects (such as droplet internal convection). Our proposed model can predict the SGHF droplet evaporation rate for its various mixing ratios up to the substrate temperature of 100 °C.

As droplet boiling involves large heat flux removal rates because of the latent heat transfer, it is imperative to study the hybrid nanofluid based droplet boiling performance. Therefore, the SGHF droplet boiling performance for its various mixing ratios and droplet volumes is investigated as another novelty of this research, which is not previously studied to our best knowledge. In this research, as the motivation to investigate the SGHF droplet evaporation and boiling performance is its spray cooling application, it is important to understand the effects of various hydrodynamic parameters (such as, the mean volumetric flux, mean droplet diameter and mean droplet velocity) on hybrid nanofluid spray cooling performance. Some researchers investigated the effects of these hydrodynamic parameters on spray cooling performance of water and dielectric fluids and also examined bubble and droplet dynamics during the spray cooling process [39–42]. However, the

spray cooling using hybrid nanofluids has not been widely investigated to date and therefore, the effects of some hydrodynamic parameters on critical heat flux (CHF) of the SGHF spray cooling is also investigated in this research. The key objectives of this paper are as follows:

- To study the mixing ratio effect on the SGHF droplet evaporation performance over heated copper and residue surfaces for sub-boiling and boiling temperatures.
- To investigate the main factors (such as the synergistic thermal conductivity and droplet internal convection) affecting the SGHF droplet evaporation rate.
- To develop an evaporation model to predict the SGHF droplet evaporation rate on heated copper and residue surfaces in a temperature range of 25°C $\leq T_s \leq$ 100 °C.

2. Experimental setup and procedure

2.1. Hybrid nanofluid synthesis and thermal characterization

The SGHF was synthesized using a two-step method for various mixing ratios (by volume) as MR-1 (0.1Ag:0.9GNP), MR-2 (0.3Ag:0.7GNP), MR-3 (0.5Ag:0.5GNP), MR-4 (0.7Ag:0.3GNP) and MR-5 (0.9Ag:0.1GNP). In a two-step method, pre-weighted graphene nanoplatelets (polycarboxylate functionalized) and silver nanoparticles (below 100 nm primary particle size, polyvinylpyrroledone stabilized), purchased from Sigma-Aldrich (USA), were mixed in deionized water and stirred using a glass rod to break large clusters. The mixture was then ultra-sonicated in an ultra-sonication bath (Model 2510, Branson, USA) for 2 hours to obtain a high dispersion stability [36,43]. The stability of the SGHF was analysed using the sedimentation technique in which the prepared SGHF samples were left undisturbed in glass test tubes. As both GNP and Ag nanoparticles were pre-stabilized using polycarboxylate functionalized groups and PVP surfactant, respectively, no traces of sedimentation were found for several hours. As hybrid nanofluids exhibit promising thermal characteristics at even low particle loading and that the main aim of this research is to study the SGHF mixing ratio effect, the particle concentration was fixed at 0.1% volume fraction. The SGHF thermal conductivity for its various mixing ratios and temperatures was subsequently investigated using a thermal constants analyser (TPS 500S, Hot Disk, Sweden). The thermal constants analyser comprises a double spiral sensor (made of Nickel) with four electrical connections. The sensor measures the resistance variations during the sample transient heating and this information is processed by the system to determine the sample thermal

conductivity. The experimental setup and procedure for thermal conductivity measurements are discussed in detail in our previous study [16]. Each measurement was performed ten times and the standard deviation was used to determine measurement uncertainties. The SGHF samples were then used in droplet evaporation and boiling experiments.

2.2. Hybrid nanofluid droplet evaporation and boiling experiments

The SGHF droplet evaporation and boiling experiments were performed in a control room at fixed ambient temperature and relative humidity of $T_a = 25 \pm 0.3$ °C and $RH = 0.3 \pm 0.03$, respectively. The (5 cm × 6 cm) copper plate was placed over a (10 cm × 15 cm) silicone heater (Model 245-629, RS PRO, UK) of 100 W power and a silicone thermal grease (Model 707-4736, RS PRO, UK) was applied on the underside of the copper plate to improve a thermal contact between the two surfaces, as illustrated in Fig. 1 (a). The T-type thermocouple was used at each end of the copper surface to monitor the copper plate surface temperature. Each thermocouple was fixed using a Teflon sheet with its each end screwed on a copper surface. The silicone heater was connected to a variable AC power supply to adjust the copper surface temperature between 25 °C and 175 °C for SGHF droplet evaporation and boiling experiments. A video camera was set up at 45° angle above the copper plate to record the SGHF droplet evaporation process at 25 frames per second. For film boiling experiments, a copper ring was used to keep the rolling SGHF droplet on a heated copper surface, as demonstrated in Fig. 1 (a). The video camera was positioned at 90° (droplet overhead) during the film boiling experiments to avoid imaging obstruction from the copper ring. Moreover, due to high evaporation dynamics in the nucleate boiling regime, a high-speed camera (HG-100K, Redlake, USA) was horizontally positioned to capture droplet images at a high frame rate in a range of 60-500 frames per second. An infrared camera (Ti25, Fluke, US) was also horizontally positioned to measure the SGHF droplet surface temperature.

Once the experimental setup was ready, the SGHF droplet was gently dispensed on a copper plate using a micropipette (F1 Finnpipette, Thermo Fisher Scientific, USA). The total evaporation time for each mixing ratio of the SGHF droplet was recorded using a video camera for droplet volumes of 3 µl, 15 µl, 30 µl, and 60 µl. Using the known droplet volume from micropipette and the total evaporation time obtained from video camera, the net droplet evaporation rate was determined as the ratio of the total droplet volume to total evaporation time. It must be noted that video camera

was used to record the total droplet evaporation time and not to obtain the droplet volume at each frame during evaporation. When the SGHF droplet completely evaporated, a residue comprising the silver-graphene hybrid nanoparticles was formed on a copper surface. Subsequently, a 3 µl volume for each mixing ratio of the SGHF droplet was gently dispensed on its respective residue surface obtained from the evaporation or boiling of the first SGHF droplet. In this way, the droplet evaporation and boiling processes for subsequent SGHF droplets were recorded for droplet volume ratios of V_{fd}/V_{sd} = 1, 5, 10 and 20, where V_{fd} is the volume of the first SGHF droplet on a copper surface and V_{sd} (fixed at 3 µl) is the volume of the second SGHF droplet on a residue surface obtained from the first evaporated SGHF droplet. Since the evaporation rate of the SGHF droplet for V_{fd}/V_{sd} = 1 is nearly the same as that for a copper surface, the subsequent droplet evaporation rate is only discussed for V_{fd}/V_{sd} = 5, 10 and 20 in Section 4 (Results and discussion). Each experiment was performed three times and the standard deviation was used to determine measurement uncertainties.

2.3. Instantaneous droplet evaporation and contact angle measurements

Besides the SGHF droplet evaporation and boiling experiments, more experiments were performed to study the instantaneous evaporation rate during the lifetime of hybrid nanofluid droplets on a heated copper substrate. These experiments were performed in an optical tensiometer (Theta, Biolin Scientific, Finland) that was calibrated using a ball calibration method prior to experiments. The copper plate (5 cm × 6 cm) was placed on an electrically heated base plate inside a small environmental chamber. The dispenser was passed through the top slit of an environmental chamber such that it reached near the heated copper surface. The target air temperature inside the environmental chamber was set in a range of 55 – 70 °C to also study the temperature effects on instantaneous droplet evaporation rate. Although the target droplet volume was set as 3 µl in the software, it was dispensed more than a preset volume for most droplets on a heated copper substrate. This may be due to high air temperature inside the environmental chamber that lowered the fluid viscosity and surface tension resulting in higher than preset volume dispensed on a heated copper plate. When the setup was ready, an automated dispenser dispensed the hybrid nanofluid droplet on a heated copper surface. As the droplet touched the surface, the camera captured the droplet images at 1.4 frames per second until the end of evaporation. In this way, the droplet volume, contact angle, contact diameter and air temperature were measured at each frame during

the droplet lifetime on a heated copper plate. The instantaneous droplet evaporation rate was determined as a ratio of change in droplet volume to time between two consecutive image frames. Moreover, the measurements were obtained for droplet contact angle up to 6° during evaporation, as the tensiometer did not accurately measure the droplet volume at very low contact angles.

2.4. Hybrid nanofluid surface tension and latent heat measurements

The surface tension for each mixing ratio of the SGHF droplet was measured in a temperature range of 20-100 °C using the same optical tensiometer as used for droplet evaporation rate and contact angle measurements. The surface tension of a 4 µl volume of the SGHF pendant droplet was measured at 1.4 frames per second for 40 seconds. The maximum mean standard deviation for all measurements of temperature and surface tension was obtained as 0.79 °C and 0.00385 N/m, respectively. The average surface tension value at different temperatures was used to determine the temperature dependent surface tension gradient for each mixing ratio of the SGHF. Moreover, the latent heat of vaporization for the SGHF was measured using a differential scanning calorimetry (Q1000, TA Instruments, USA). The pre-weighted SGHF samples were heated in a temperature range of 20 – 200 °C at a heating rate of 10 °C/min to determine the latent heat of vaporization. Each experiment was performed three times and measurement uncertainties were determined using the standard deviation of the mean value.

2.5. Hybrid nanofluid spray cooling experiments

The silver-graphene hybrid nanofluid (SGHF) spray cooling setup is demonstrated in Fig. 1 (b). A cartridge heater was inserted in a copper heater block and four T-type thermocouples (T_1, T_2, T_3 and T_4) were used to measure the temperature along the heater head, as illustrated in Fig. 1 (b). The heater block and heater head were insulated using a superwool insulation. The 0.1% volume fraction of SGHF from the storage tank was pumped (Model: 083942, Xylem Flojet, UK) and sprayed on a heater spray surface. The SGHF droplets upon impact with the heater spray surface formed a hot stream that was cooled using the plate heat exchanger before it entered the storage tank. The heater was instantly turned-off following the critical heat flux to prevent system failure due to temperature overshoot. The heat flux ($Q = kA\Delta T/\Delta x$) was determined using the temperature data from two successive thermocouples. In this way, three heat fluxes (Q_1, Q_2 and Q_3) were obtained using the temperature data from four thermocouples (T_1 T_2, T_3 and T_4) that were averaged

to obtain the mean heat flux. The Sauter mean droplet diameter ($d_{32}=\sum N_i d_i^3/\sum N_i d_i^2$, where N_i is the number of spray droplets having diameter d_i) and maximum droplet velocity (V_{max}) were obtained using interferometric Mie imaging (IMI) and particle image velocimetry (PIV) techniques, respectively. The Sauter mean diameter (d_{32}) was obtained from the spray droplet size distribution that was developed by processing 90 images at 5 frames per second using an IMI setup. Moreover, V_{max} was obtained from the mean velocity field developed by processing 10 images at 5 frames per second using a PIV setup.

3. Numerical modelling

A numerical model to investigate the internal convection effect (thermal Marangoni and natural convection) on flow field and temperature profile inside an evaporating SGHF droplet was developed using COMSOL Multiphysics. The numerical model gives freedom to separately study the quantitative effects of Marangoni and natural convection forces, which is difficult to investigate experimentally, where both Marangoni and natural convection processes simultaneously occur within an evaporating droplet. Due to the geometric symmetry of a sessile droplet, a 2-D axisymmetric space dimension with non-isothermal laminar flow interface was used to build our model. A 2-D axisymmetric droplet geometry was developed by determining the x and y coordinates for different points along the droplet (spherical cap) surface. The droplet contact angle was determined by post-processing the actual droplet image using ImageJ. The continuity equation for a steady state incompressible SGHF droplet solved in this numerical model can be written as:

$$\rho \nabla . V = 0 \tag{1}$$

where ρ is the density and V is the velocity of the SGHF. The numerical model also solves the momentum conservation equation given as:

$$\rho(V.\nabla V) = -\nabla p + \nabla.\left(\mu(\nabla V + (\nabla V)^T) - \frac{2}{3}\mu(\nabla . V)\right) + \rho g \tag{2}$$

where p is the pressure and μ is the dynamic viscosity of the SGHF. The heat transfer in this numerical setup is modelled by solving the energy conservation equation and can be written as:

$$\rho C_p V.\nabla T = \nabla.(k\nabla T) + Q + Q_p + Q_{vd} \tag{3}$$

where C_p is the specific heat capacity and k is the thermal conductivity of the considered SGHF. Moreover, Q, Q_p and Q_{vd} are the energy generation, pressure and viscous dissipation terms,

respectively. The SGHF thermo-physical properties (such as k, μ, ρ and C_p) were used to define the material properties for the SGHF droplet. The thermophysical properties, such as viscosity (μ), density (ρ) and specific heat capacity (C_p) were obtained from well-established models that can closely predict these properties for hybrid nanofluids [16,20]. However, the existing thermal conductivity (k) models do not correctly predict the thermal conductivity for various mixing ratios of the SGHF used in this study (discussed in Section 4.1). Therefore, in this numerical model, we focused on the thermal conductivity k for the SGHF droplet, which was obtained using a semi-empirical model developed in this study, as discussed in Section 4.1. The copper surface temperature was used at droplet base as a boundary condition, while the measured droplet surface temperature from infrared thermal images (as discussed in the supplementary material) was used to define the droplet-air interface temperature as a boundary condition in our numerical model. A no-slip boundary condition was used at the droplet base while a slip boundary condition was used at the droplet-air interface. Moreover, the Marangoni effect was used as a boundary condition at droplet-air interface of the SGHF droplet in this numerical model. The measured surface tension gradient for each mixing ratio of the SGHF (as illustrated in Fig. 2 (a)) was used as an input parameter in the model. In order to examine to effect of Marangoni convection, the model was solved twice under the same conditions, initially without the Marangoni effect and later with the Marangoni effect. In this way, the flow field and temperature distribution inside the SGHF droplet was examined in the presence and absence of thermal Marangoni convection, as discussed in Section 4. The particle-tracing module was used to simulate the hybrid nanoparticles inside the SGHF droplet. Due to a simple 2-D droplet geometry, the free triangular mesh was used in our model. In this study, as the internal flow was investigated at the start of droplet evaporation for a fixed time of t = 2s, a stationary solver was used with relative tolerance of 10^{-5}.

3.1. Model validation and mesh independence test

The mesh independence test was performed on a 30 µl SGHF droplet volume for elements ranging from coarse (538 elements) to extra fine (13733) mesh elements, as shown in Fig. 1 (c). It was noticed that the results were considerably improved when the mesh density was increased from 538 (coarse) elements to 5407 (finer) elements. However, further increasing the mesh density to 13733 (extra fine) elements had a negligible effect on the velocity magnitude. Therefore, to

improve the computational effectiveness of our model, the extra-fine mesh was used near the droplet boundaries while finer mesh was used in the rest of the droplet domain.

As demonstrated in Fig. 1 (d), the numerical model for water droplet was validated using the PIV experimental data on internal flow in a heated water droplet recently studied by Karlsson et al. [44]. The validation was performed using the same droplet parameters and experimental conditions as used by Karlsson et al. [44] in their investigation. As water droplet used in their experiments had a contact radius below the capillary length, the sessile water droplet was assumed as a spherical cap. Based on this assumption, the droplet height and contact radius data was used to determine the droplet surface coordinates, which were subsequently used to develop the droplet geometry. Fig. 1 (d) illustrates the mean velocity magnitude along the droplet height for time $t = 20 - 50$ s during the droplet evaporation at substrate temperatures of 313.13 K and 323.13 K. It is observed that our numerical model predicts the velocity profile with reasonable accuracy for both substrate temperatures. However, small mean deviation of 8% for 313.13 K plots and 10% for 323.13 K plots may be due to the model simplifications, such as neglecting evaporation effects from the droplet surface or thermal plume effects from the heated surface around an evaporating droplet.

4. Results and discussion

4.1. Effect of mixing ratio on the SGHF thermal conductivity and droplet evaporation rate

The effect of mixing ratio on the SGHF thermal conductivity at different temperatures is illustrated in Fig. 2 (b). Along *x*-axis, the mixing ratio increases with respect to Ag nanoparticle concentration, where zero corresponds to GNP nanofluid and one corresponds to Ag nanofluid. It is noticed that the MR-2 SGHF gives the highest measured thermal conductivity among considered mixing ratios at all studied temperatures. This may be due to the synergistic effect induced by inter-particle compatibility and a thermal pathway between suspended Ag and GNP nanoparticles in MR-2 SGHF. It is observed that the thermal conductivity enhancement of MR-2 SGHF with respect to the base fluid (water) is augmented from 2% to 8% with increasing temperature from 20 °C to 70 °C. This is a reasonable enhancement considering a low particle loading of 0.1% volume fraction in this study. Since silver (Ag) nanoparticles are spherical in shape while graphene nanoplatelets (GNP's) have a planer structure, the synergistic thermal properties are achieved when spherical Ag nanoparticles come in contact with the planer surface of GNP's creating a

thermal network with synergistic effects. Moreover, as the in-plane thermal conductivity of GNP's is about 10 times that of Ag nanoparticles [27,45], the synergistic thermal conductivity is achieved for a mixing ratio of MR-2 (0.3Ag:0.7GNP) in current study, where GNP's have a higher concentration by volume than Ag nanoparticles. Fig. 2 (b) also shows that the modified Maxwell model cannot be used to estimate the SGHF thermal conductivity and it largely under-predicts our experimental data, as also reported by Takabi and Salehi [46]. They transformed the classical Maxwell model (originally developed for single particle nanofluids) into the following modified Maxwell model for hybrid nanofluids:

$$k_{mod,Maxwell} = k_w \left[\frac{\frac{\emptyset_{Ag} k_{Ag} + \emptyset_{GNP} k_{GNP}}{\emptyset} + 2k_w + 2(\emptyset_{Ag} k_{Ag} + \emptyset_{GNP} k_{GNP}) - 2\emptyset k_w}{\frac{\emptyset_{Ag} k_{Ag} + \emptyset_{GNP} k_{GNP}}{\emptyset} + 2k_w - (\emptyset_{Ag} k_{Ag} + \emptyset_{GNP} k_{GNP}) + \emptyset k_w} \right] \quad (4)$$

where $\emptyset$ is the volume fraction, $\emptyset_{Ag} = MR\emptyset$, $\emptyset_{GNP} = (1 - MR)\emptyset$ and k_w, k_{Ag} and k_{GNP} are the thermal conductivities of water, Ag nanoparticle and graphene nanoplatelet (GNP), respectively. Takabi and Salehi [46] also found that their modified Maxwell model could not correctly predict the experimental data on hybrid nanofluid thermal conductivity. Therefore, we transform the modified Maxwell model into a semi-empirical model by using our experimental data for the SGHF thermal conductivity and is given as:

$$k_{SGHF} = C k_{mod,Maxwell} \quad (5)$$

where the coefficient C depends on the SGHF mixing ratio (MR) and temperature (T) and is determined as:

$$C = 0.992 + 0.1694MR - (0.2981MR^2) + 0.0172\left(\frac{T - T_o}{T_o}\right)^2 + 0.1296MR^3 - 0.00354\left(\frac{T - T_o}{T_o}\right)^3 \quad (6)$$

where T_o is the reference temperature equal to 20 °C, as it is the lowest temperature at which the thermal conductivity was measured for SGHF samples. Equation (6) is the non-hierarchical polynomial function containing all significant variables (p value < 0.05) with coefficient of determination as R^2 = 91%. Fig. 2 (b) illustrates that the proposed semi-empirical model in equation (5) can estimate the SGHF thermal conductivity with better accuracy than the modified Maxwell model [46]. By solving equation (6) for $dC/dMR = 0$, we can find the optimum mixing ratio of MR_{opt} = 0.38 that gives the highest thermal conductivity for the SGHF at all studied temperatures, as also shown in Fig. 2 (b). The thermal conductivity trend from our semi-empirical model (dashed lines in Fig. 2 (b)) shows that it increases with increasing mixing ratio from 0 (GNP nanofluid) to 0.38 (MR_{opt}) and then decreases up to the mixing ratio of 1 (Ag nanofluid). The

developed semi-empirical model can be further improved by incorporating other hybrid nanofluids for a wide range of particle volume fraction.

The instantaneous evaporation rate for different mixing ratios and initial volumes (V_i) of the SGHF droplet on a heated copper surface is illustrated in Fig. 2 (c). It can be noticed that all SGHF droplets exhibit a quasi-steady evaporation rate, where the evaporation rate varies slowly during the droplet lifetime on a heated copper surface. Furthermore, the initial transient period during the droplet warm-up time is not observed in Fig. 2 (c). This may be due to a very short time-scale for initial transient period of small sized droplets considered in this study. Also, the transient effects near the end of droplet evaporation are not observed in Fig. 2 (c), possibly because measurements were not obtained for droplet contact angles below 6° (as discussed in Section 2.3). It must be noted that the instantaneous evaporation rate in Fig. 2 (c) cannot be compared to the evaporation rate shown in Fig. 3, as these measurements were performed under different conditions and using different experimental setups. Fig. 2 (d) demonstrates the corresponding contact angles and contact diameters of evaporating SGHF droplets on a heated copper surface. It can be noticed that contact angle varies in a similar manner for all studied mixing ratios of the SGHF droplet. Moreover, due to the pinning effect induced by particle deposition during the SGHF droplet evaporation, the droplets exhibit constant contact diameter on a heated copper surface, as illustrated in Fig. 2 (d).

Fig. 3 (a-d) shows the evaporation rate for different mixing ratios and volumes of the SGHF droplet on a copper surface in a temperature range of 25-100 °C. For same droplet volume, almost the same droplet evaporation rate is obtained for all SGHF mixing ratios on an un-heated copper surface (i.e., $T_s = T_a = 25$ °C). This is because droplet evaporation on an un-heated copper surface mainly occurs due to the mass diffusion from droplet surface that is not affected by the SGHF mixing ratio, as discussed in detail in our recent research [36]. However, as the copper surface is heated, variation in droplet evaporation rate is observed for different mixing ratios of the same volume of the SGHF droplet. Despite highest measured thermal conductivity for MR-2 SGHF (as shown in Fig. 1 (d)), it is observed that GNP nanofluid and MR-1 SGHF droplets give highest evaporation rates for all studied droplet volumes (3 µl, 15 µl, 30 µl and 60 µl) on a heated copper surface among all considered mixing ratios. This suggests that other physical factors, such as the droplet internal convection, also affect the SGHF droplet evaporation rate that will be further

discussed in section 4.1.1. Fig. 3 (a-d) shows that enhancement in evaporation rates up to 93%, 55%, 52% and 62% can be obtained by using low mixing ratio SGHF droplets (MR ≤ 0.1, i.e., GNP and MR-1) as compared to high mixing ratio droplets (MR ≥ 0.9, i.e., MR-5 and Ag) for droplet volumes of 3 µl, 15 µl, 30 µl and 60 µl, respectively. The relatively low evaporation rates of high mixing ratio SGHF droplets may be due to their low thermal conductivity, as illustrated in Fig. 1 (d). Furthermore, the evaporation rate in low mixing ratio SGHF droplets (MR ≤ 0.1, i.e., GNP and MR-1) increases up to 218% with increasing droplet volume from 3 µl to 60 µl.

Fig. 4 (a-c) shows a comparison in evaporation rate of a 3 µl SGHF droplet for its various mixing ratios on a copper surface and respective residue surfaces (V_{fd}/V_{sd} = 5, 10 and 20) in a temperature range of 25-100 °C. It is observed that the SGHF droplet exhibits enhanced evaporation performance on its heated residue surface as compared to the heated copper surface for all mixing ratios. This is because the heated residue surface has a higher wettability than a heated copper surface. High residue wettability increases the effective heat exchange area at droplet-solid interface, resulting in high kinetic energy liquid molecules reaching the droplet-air interface from high temperature droplet-solid interface due to droplet internal convection currents. The high kinetic energy liquid molecules on reaching the droplet-air interface leave the droplet surface resulting in high evaporation rates. The SGHF droplet residue wettability for its different mixing ratios is discussed in detail in our recent study [36]. Moreover, increasing the residue size (droplet volume ratio) from V_{fd}/V_{sd} = 5 to V_{fd}/V_{sd} = 20 increases the subsequent droplet evaporation rate in a range of 32 − 73%, as shown in Fig. 4 (a-c). This is because the droplet spreading on a wetted residue surface increases with increasing residue size. Following a similar trend of droplet evaporation on a copper surface, the low mixing ratio SGHF droplets (MR ≤ 0.1, i.e., GNP and MR-1) exhibit highest evaporation rates on their respective residue surfaces among all considered mixing ratios. This enhancement in evaporation rate is due to the coupled effect of their enhanced thermal conductivity and highly wetted residue surfaces as compared to partially wetted residue surfaces for other mixing ratios. More details of residue wetting effects on pinning or de-pinning of subsequent hybrid nanofluid droplets can be found in our recent studies [17,36]. Another reason for high evaporation rates in low mixing ratio droplets may be the internal convection effects induced by thermo-capillary (thermal Marangoni convection) or thermo-gravitational (natural convection) forces, which is discussed in the next section 4.1.1.

4.1.1. Internal convection effects in the SGHF droplet over a heated surface

In order to understand the relative strength of thermal Marangoni and natural convection forces within the SGHF droplet on heated surfaces, the dynamic Bond number [$Bo_d = Ra/Ma = \rho g \beta R^2/(-d\gamma/dT)$] is studied for different droplet volumes and residue sizes, as shown in Fig. 5 (a, b). For determining the dynamic Bond number of the SGHF droplet, the surface tension gradient ($d\gamma/dT$) was obtained from Fig. 2 (a), while the volumetric expansion coefficient and the density were determined as $\beta = -1/\rho(d\rho/dT)$ and $\rho = MR\phi\rho_{Ag} + (1-MR)\phi\rho_{GNP} + (1-\phi)\rho_w$, respectively, where both β and ρ were evaluated at $T = (T_a + T_s)/2$. It is noticed in Fig. 5 (a) that the dynamic Bond number increases with increasing copper surface temperature and droplet volume, thereby suggesting an increase in natural convection forces. However, the thermal Marangoni forces still dominate the natural convection forces for studied droplet volumes and surface temperatures, as the dynamic Bond number is below 1 (i.e., $Bo_d < 1$). Moreover, the dynamic Bond number in low mixing ratio SGHF droplets (MR ≤ 0.1, i.e., GNP and MR-1) is lower than that of high mixing ratio droplets (MR ≥ 0.9, i.e., MR-5 and Ag). This shows that the relative magnitude of thermal Marangoni forces are higher in low mixing ratio SGHF droplets as compared to high mixing ratio droplets. This may be a reason for higher evaporation rates in low mixing ratio droplets as compared to high mixing ratio droplets on a heated copper surface, as shown in Fig. 3 (a-d).

Fig. 5 (b) illustrates the dynamic Bond number of a subsequent 3 µl SGHF droplet on its residue surface for different residue sizes and substrate temperatures. It is noticed that the dynamic Bond number tremendously increases for low mixing ratio SGHF droplets with increasing residue size from $V_{fd}/V_{sd} = 5$ to $V_{fd}/V_{sd} = 20$. This is because the low mixing ratio droplets show higher spreading on their extremely wetted residue surfaces than high mixing ratio droplets on their less wetted residue surfaces (discussed in our previous study [36]). Although thermo-gravitational forces increase in low mixing ratio droplets due to increase in the dynamic Bond number with increasing residue size, the Marangoni forces still dominate the natural convection forces, as $Bo_d < 1$. The results in Fig. 5 (a) and (b) suggest that the thermal Marangoni convection may be a key factor affecting the SGHF droplet evaporation on both heated copper and residue surfaces. However, the relative effect of the thermal Marangoni and natural convection on the SGHF droplet internal flow field and temperature distribution should also be investigated.

Fig. 5 (c) and (d) demonstrate the internal flow field and temperature distribution in the SGHF droplet, respectively, when both Marangoni and natural convection are considered (droplet left half) as compared to the case when only natural convection is considered (droplet right half) for a copper surface temperature of T_s = 60 °C. The Ag nanoparticles are shown by blue particles and the graphene nanoplatelets (GNP) are represented by pink particles. In Fig. 5 (c), it is observed that the velocity magnitude in the combined Marangoni and natural convection induced flow is about two orders of magnitude to that induced by only natural convection. This suggests that thermal Marangoni forces dominate natural convection forces inside the studied SGHF droplet. Fig. 5 (d) illustrates that the average droplet internal temperature due to combined thermal Marangoni and natural convection (droplet left half) is lower than that obtained from only natural convection (droplet right half). This is because relatively high fluid velocity achieved from dominating Marangoni convection generates a well-mixed internal flow, resulting in high droplet near-wall (droplet-solid interface) temperatures and relatively low temperature in the rest of the flow domain, as demonstrated in droplet left half of Fig. 5 (d). Conversely, extremely low fluid velocity in natural convection induced flow domain results in thermally stratified layers signifying poor flow mixing effects, as shown in droplet right half of Fig. 5 (d). These results indicate that a well-mixed flow field mainly induced by thermal Marangoni convection rapidly transports the hot fluid from droplet-solid interface to droplet-air interface, resulting in high droplet evaporation rates over heated surfaces. Although Stokes-Einstein diffusivity increases with temperature, our numerical model suggests that the Brownian motion of suspended hybrid nanoparticles have a negligible effect on velocity and thermal fields of the SGHF droplet over a heated copper substrate. This may be because thermophoretic forces dominate Brownian forces due to the temperature gradient between the droplet-solid interface and the droplet-air interface. Some researchers also suggested that thermophoresis dominate the Brownian diffusion up to two orders of magnitude in a heated nanofluid system [47,48]. Moreover, it should be noted that the droplet image in Fig. 5 (d) shows the droplet internal temperature distribution, while the infrared thermal images in supplementary material exhibit the droplet surface temperature distribution. For this reason, the droplet temperature distribution from our model (Fig. 5 (d)) cannot be compared to that obtained from infrared thermal images.

Fig. 6 shows the separate effects of Marangoni and natural convection forces on velocity magnitude along the droplet height (y/h) in SGHF droplets at the start of droplet evaporation (t = 2s) for copper surface temperature of T_s = 60 °C. The results show that the velocity magnitude induced by thermal Marangoni convection is about 2−3 orders of magnitude the velocity induced by natural convection for all studied droplet volumes in a range of 3−60 µl. This further suggests that the thermal Marangoni forces dominate the natural convection forces in evaporating SGHF droplets, as also shown in Fig. 5 (a-d). Fig. 6 insets show that velocity magnitude along the droplet height in low mixing ratio droplets (MR ≤ 0.1, i.e., GNP and MR-1) is higher than in high mixing ratio droplets (MR ≥ 0.9, i.e., MR-5 and Ag). This suggests the presence of relatively large thermal Marangoni forces in low mixing ratio droplets that may be the reason for their higher evaporation rates than high mixing ratio droplets (as shown in Fig. 3). In Fig. 6, the internal convection effects in SGHF droplets is only shown for T_s = 60 °C, however, it is suggested that the thermal Marangoni convection still dominates the natural convection for T_s > 60 °C. This is demonstrated in Fig. 5 (a, b) by low dynamic Bond number values (Bo_d < 1) for T_s > 60 °C.

4.1.2. Development of a diffusion-convection evaporation model for the SGHF droplet

In a purely diffusive evaporation process, high evaporation rates near the droplet three-phase contact line may lead to a coffee-ring residue pattern. However, in this research, uniform residue patterns were observed from evaporation of all mixing ratios of SGHF droplets for copper surface temperatures up to 100 °C. Moreover, the diffusion evaporation models based on the Fick's law of mass diffusion, when applied for droplets resting on heated surfaces, under-predict the measured droplet evaporation rates. Research indicates that deviation between the experimental droplet evaporation rate and that predicted by the diffusion model is 100% at $(T_s - T_a)/T_a$ = 1.8 [37,38]. This suggests that droplet evaporation on heated surfaces is contributed by both diffusive as well as convective processes. Moreover, the dynamic bond number and the droplet internal velocity and thermal fields in Fig. 5 (a-d) further indicate that thermal Marangoni forces much dominate the natural convection forces. Therefore, the net evaporation rate of the SGHF droplet on a heated surface is a combined effect of the mass diffusion and the thermal Marangoni convection and is given by the following equation:

$$E = E_D + E_{MC}\ , \tag{7}$$

where E_D and E_{MC} are the droplet evaporation rates due to the mass diffusion and the thermal Marangoni convection, respectively. The first term in equation (7) is the diffusion evaporation rate (in µl/s) that can be obtained from the Fick's law of mass diffusion as:

$$E_D = J_o \pi MCDR(x_{v,2} - x_{v,1})/\rho\,, \tag{8}$$

where $x_{v,1} = P_{sat}/P_a$ is the vapor mole fraction at droplet-air interface and is defined as the ratio of vapor saturation pressure (P_{sat}) to ambient air pressure (P_a), $x_{v,2} = RHx_{v,1}$ is the vapor mole fraction in surrounding ambient air (where RH = 0.3), R is the droplet contact radius and ρ is the water density. The reason for considering water density instead of the SGHF density is that the evaporated mass from the SGHF droplet only comprises water molecules while leaving a residue of hybrid nanoparticles on a copper substrate at the end of evaporation. The molar concentration (C) and mass diffusivity (D) of evaporating droplets were determined at an average temperature of substrate and ambient air temperatures. The semi-empirical term J_o is an evaporation constant that is a function of the non-dimensional droplet contact radius (R/R_o) for a copper surface, while it depends on the mixing ratio (MR) and the droplet volume ratio (V_{fd}/V_{sd}) for a residue surface and is determined as:

$$J_o = a_o + \sum_{i=1}^{2} a_i \left(\frac{R}{R_o}\right)^i \text{ (Copper surface)}, \tag{9}$$

where a_o = 4.643, a_1 = -3.455, a_2 = 0.804 and R_o is the contact radius of the smallest droplet volume of 3 µl considered in this study.

$$J_o = \sum_{j=1}^{3} b_j \left(\frac{V_{fd}}{V_{sd}}\right)^j + \sum_{k=2}^{5} c_k (MR)^k \text{ (Residue surface)}, \tag{10}$$

where b_1 = 0.6707, b_2 = -0.067, b_3 = 0.0019, c_2 = -27.533, c_3 = 117.456, c_4 = -174.116 and c_5 = 85.148. It must be noted that all coefficients in equations (9) and (10) were obtained using the experimental data on the SGHF droplet evaporation rate (as shown in Fig. 3) for unheated substrate (i.e., $T_s = T_a$ = 25 °C). Equation (9) is the quadratic equation with coefficient of determination as R^2 = 99.4%, while equation (10) is the non-hierarchical polynomial function containing all significant variables (p value < 0.05) with coefficient of determination as R^2 = 98.7%. The second unknown term in equation (7) is the evaporation rate due to the thermal Marangoni convection (E_{MC}). Equation (7) is re-arranged to obtain the non-dimensional form of the Marangoni convection induced evaporation rate (E_{MC}/E_D) that is the function of the Marangoni number (Ma) and is given as:

$$E_{MC}/E_D = (E/E_D) - 1 = f(Ma) = C_o Ma\,, \tag{11}$$

where $Ma = R\Delta T[(-d\gamma/dT)(\rho C_p/\mu k)]_{SGHF}$ and $\Delta T = T_s - T_a$. The term $d\gamma/dT$ is the surface tension gradient for the SGHF and is obtained from Fig. 2 (a). The SGHF thermal conductivity (k) is obtained from equation (5) while the parameters ρ, C_p and μ for the SGHF are determined from the hybrid nanofluid classical models [16,20]. E_{MC}/E_D in equation (11) is determined using our experimental data for the net evaporation rate (E) and equation (8) for diffusion evaporation rate (E_D). In equation (11), there exists a linear relationship between the terms E_{MC}/E_D and Ma that can be estimated by a straight-line equation with y-intercept equal to zero (as discussed in the supplementary material). The coefficient C_o in equation (11) is a function of the SGHF mixing ratio (MR) and the dimensionless contact radius (R/R_o) for a copper surface, given as:

$$C_o = \sum_{l=1}^{3} d_l (R/R_o)^l + \sum_{m=1}^{2} e_m (MR)^m \quad \text{(Copper surface)}, \tag{12}$$

where $d_1 = 0.000205$, $d_2 = -0.0001$, $d_3 = 0.000013$, $e_1 = -0.000066$ and $e_2 = 0.000047$. Equation (12) is a polynomial function containing all significant variables (p value = 0) with coefficient of determination as $R^2 = 99.8\%$. For residue surfaces, equation (8) is highly sensitive to the coefficient C_o, therefore, C_o is estimated as a high order polynomial function of mixing ratio (MR) and determined as:

$$C_o = \begin{cases} x_o + \sum_{n=1}^{6} x_n (MR)^n \Rightarrow V_{fd}/V_{sd} = 5 \\ y_o + \sum_{p=1}^{6} y_p (MR)^p \Rightarrow V_{fd}/V_{sd} = 10 \\ z_o + \sum_{q=1}^{6} z_q (MR)^q \Rightarrow V_{fd}/V_{sd} = 20 \end{cases} \quad \text{(Residue surface)}, \tag{13}$$

where $x_o = 0.000073$, $x_1 = -0.000853$, $x_2 = 0.013325$, $x_3 = -0.066434$, $x_4 = 0.143436$, $x_5 = -0.139602$, $x_6 = 0.050341$, $y_o = 0.000044$, $y_1 = -0.000342$, $y_2 = 0.006254$, $y_3 = -0.031893$, $y_4 = 0.069993$, $y_5 = -0.070106$, $y_6 = 0.026412$, $z_o = 0.000043$, $z_1 = -0.00085$, $z_2 = 0.016384$, $z_3 = -0.090322$, $z_4 = 0.210715$, $z_5 = -0.2192$ and $z_6 = 0.08389$. In equation (13), the coefficient of determination obtained for all considered residues sizes is equal to $R^2 = 1$. Substituting E_d from equation (8) in equation (11) and re-arranging it gives the following relation for the SGHF net droplet evaporation rate:

$$E = J_o \pi MCDR\left(x_{v,2} - x_{v,1}\right)(1 + C_o Ma)/\rho. \tag{14}$$

Although the developed diffusion-convection model (equation (14)) closely estimates the SGHF droplet evaporation rate on heated copper and residue surfaces, it also predicts the droplet evaporation rate between the measured data points, as shown in Fig. 3 and Fig. 4.

4.2. Effect of mixing ratio on the SGHF droplet boiling

Fig. 7 (a-d) shows the evaporation rate for different mixing ratios of SGHF droplets on a copper surface in three distinct boiling regimes, i.e., the nucleate boiling, transition boiling and film boiling. In Fig. 7 (a), the critical point (C_p) is defined as the temperature where the droplet nucleate boiling ends and transition boiling starts. The critical point is significantly important in thermal applications, where the cooling process is maintained below the critical point in the nucleate boiling regime to achieve high heat removal rates. As temperature exceeds the critical point, the transition boiling occurs, where the droplet evaporation rate drastically drops and the required heat may not be removed eventually resulting in device failures. Unlike droplet evaporation for surface temperatures up to T_s = 100 °C, where low mixing ratio droplets ($MR \leq 0.1$) gave highest evaporation rates (as shown in Fig. 3 and Fig. 4), a reverse behaviour is noticed in the nucleate boiling regime, where high mixing ratio droplets ($MR \geq 0.9$) gave highest evaporation rates. This is because high mixing ratio SGHF droplets expand more than low mixing ratio droplets (as discussed in the supplementary material) during boiling on a heated copper surface due to the high concentration of thermally conductive Ag nanoparticles. The highly energetic Ag nanoparticles transfer their energy to surrounding water molecules inducing droplet agitation and eruption that results in higher droplet expansion in high mixing ratio droplets as compared to low mixing ratio droplets. The droplet expansion increases the droplet-solid interfacial heat exchange area resulting in enhanced evaporation rates in high mixing ratio SGHF droplets.

At the critical point C_p ($T_s \approx$ 125 °C), the droplet evaporation rate is almost the same for all SGHF mixing ratios. This is because all mixing ratios of SGHF droplets undergo intense agitation and eruption and therefore exhibit short life spans. Also, due to intense heat at the critical point C_p ($T_s \approx$ 125 °C), the droplets exhibit little expansion over the copper surface (as discussed in the supplementary material) that results in almost the same evaporation rate for both low and high mixing ratio droplets. In Fig. 7 (a-d), at the critical point C_p, the droplet evaporation rate for SGHF droplet volumes of 15 µl, 30 µl and 60 µl increases up to 112%, 256% and 620% as compared to 3 µl droplet volume. Following the critical point C_p, in the transition boiling regime, the droplet evaporation rate starts decreasing with high mixing ratio droplets ($MR \geq 0.9$) exhibiting a sharper decline than low mixing ratio droplets ($MR \leq 0.1$). Following the Leidenfrost point L_p, in the film-boiling regime, the SGHF droplets almost give the same evaporation rate irrespective of their

mixing ratio. This is because the droplet has a minimal contact area due to the vapour cushion separating it from the heated surface, as shown in Fig. 7 (a) inset. The boiling dynamics of both low and high mixing ratio SGHF droplets is discussed in the supplementary material.

Fig. 8 (a-c) shows a comparison in evaporation rate for various mixing ratios of a 3 µl SGHF droplet on both copper and residue surfaces in the nucleate boiling regime (103 °C ≤ T_s ≤ 125 °C). It is observed that the SGHF droplet on its wetted residue surface gives enhanced evaporation rates as compared to the non-wetted copper surface, exhibiting maximum enhancement at T_s = 115 °C. However, the droplet evaporation trend with respect to the mixing ratio on a residue surface is not clear for V_{fd}/V_{sd} = 5 and V_{fd}/V_{sd} = 10. This is because the first boiling droplet abruptly erupts small-sized droplets resulting in a non-uniform residue surface. However, for V_{fd}/V_{sd} = 20, low mixing ratio droplets (MR ≤ 0.1) show higher evaporation rates than high mixing ratio droplets (MR ≥ 0.9) on their respective residue surfaces. This is because low mixing ratio droplets exhibit large spreading on their extremely wetted residue surfaces as compared to high mixing ratio droplets on their less wetted residue surfaces, as demonstrated in Fig. 8 (d). Large droplet spreading (large contact diameter) increases the droplet-solid heat exchange area that results in high evaporation rates. However, at T_s = 115 °C, despite smaller contact area on a residue surface than on a copper surface (as demonstrated in Fig. 8 (d)), the MR-5 droplet exhibits higher evaporation rate on a residue surface than on a copper surface, as illustrated in Fig. 8 (c). This may be because other factors, such as, the MR-5 residue thermal conductivity or capillary effect across residue pores, increase the evaporation rate of the subsequent MR-5 droplet on its own residue surface. Also, the subsequent 3 µl SGHF droplets give similar evaporation rates for studied residue sizes of V_{fd}/V_{sd} = 5, V_{fd}/V_{sd} = 10 and V_{fd}/V_{sd} = 20 due to non-uniform residue surfaces. Furthermore, as the SGHF droplet rolls over the copper surface due to the reduced surface contact area in transition and film boiling regimes, the subsequent droplet evaporation rate is only investigated up to the critical point (C_p) in the nucleate boiling regime.

Fig. 9 (a) illustrates the latent heat flux of low (MR-1) and high mixing ratio (MR-5) droplets over heated copper and residue surfaces in the nucleate boiling regime. The latent heat flux is determined as $Q = \rho E h_{fg}/A_c$, where E is the droplet evaporation rate, h_{fg} is the latent heat of vaporization ($h_{fg,MR\text{-}1}$ =2207.8±47.2 kJ/kg and $h_{fg,MR\text{-}5}$ =2325.5±31.7 kJ/kg), A_c is the droplet-solid

682 contact area and ρ is the water density (as the evaporated mass only comprises water molecules
683 while leaving the residue on heated surface). The droplet-solid contact area (A_c) was measured
684 from the residue size at the end of the droplet boiling process. Based on propagation of error for
685 all measured data, the mean standard deviation was obtained for droplet latent heat flux, as shown
686 by error bars in Fig. 9 (a). It can be noticed that the latent heat flux for MR-5 droplets is higher
687 than MR-1 droplets due to their enhanced evaporation rates (as demonstrated in Fig. 7) and high
688 latent heat of vaporization. Despite an increase in evaporation rate with increasing droplet volume
689 in the nucleate boiling regime (as illustrated in Fig. 7), the latent heat flux generally decreases with
690 increasing droplet volume. This is due to the small contact area (A_c) of small droplets that results
691 in their high latent heat flux. However, a few large droplets exhibit higher heat flux due to their
692 much higher evaporation rates than small droplets, as shown in Fig. 9 (a). Furthermore, MR-5
693 droplets show higher heat flux than MR-1 droplets on their respective residues during the nucleate
694 boiling. Besides high latent heat of vaporization for the MR-5 droplet, high latent heat flux is also
695 due to the small contact area of the MR-5 droplet as compared to the MR-1 droplet on their
696 respective residues, as demonstrated in Fig. 8 (d). The highest latent heat flux of 890 W/cm^2 and
697 850 W/cm^2 are obtained for a 3 µl volume of MR-5 droplet on copper and residue surfaces,
698 respectively, at the critical point (C_p) of $T_s \approx 125$ ℃.
699
700 Fig. 9 (b) illustrates the effects of spray mean volumetric flux along with the Sauter mean droplet
701 diameter (d_{32}) and maximum droplet velocity (V_{max}) on the critical heat flux (CHF) of MR-1 and
702 MR-5 SGHF spray cooling. It can be noticed that increasing the spray mean volumetric flux
703 increases the Sauter mean diameter and maximum droplet velocity for the spray cooling setup
704 developed in this research. It is observed that increasing the mean volumetric flux from 0.01
705 m^3/m^{2}s to 0.019 m^3/m^{2}s decreases the CHF by 8.6% for MR-1 spray cooling. However, a reverse
706 trend is noticed for MR-5 spray cooling, where the CHF increases by 87%. This suggests that high
707 heat dissipation flux can be removed from high heat flux devices using the MR-5 SGHF spray at
708 the mean volumetric flux of 0.019 m^3/m^{2}s. Moreover, the reverse effect of mean volumetric flux
709 on the CHF of MR-1 and MR-5 spray cooling may be due to the residue deposition during the
710 SGHF spray cooling process. The deposited residues (as shown in Fig. 9 (b) insets) for MR-1 and
711 MR-5 sprays may have different surface properties (such as, roughness, porosity and thermal
712 conductivity) that may have different effect on the CHF of MR-1 and MR-5 spray cooling.

5. Conclusions

In recent years, many high heat-dissipating devices challenged the cooling ability of existing thermal fluids. The performance of these devices highly depends on cooling efficiency, which may lead to device failures in extreme conditions. To address this concern, we studied the evaporation and boiling behaviour for various mixing ratios of the silver-graphene hybrid nanofluid (SGHF) droplet on heated copper and their own residue surfaces. We investigated effects of the synergistic thermal conductivity and the thermal Marangoni convection on evaporation performance of the SGHF droplet over heated surfaces. Based on our experimental and numerical findings, we developed a diffusion-convection evaporation model that can predict the SGHF droplet evaporation rate on heated surfaces in a temperature range of 25°C $\leq T_s \leq$ 100 °C. Our results showed that the SGHF droplet evaporation and boiling performance highly depend on its mixing ratio. However, in the film-boiling regime, the mixing ratio has a negligible effect on the SGHF droplet evaporation rate. Furthermore, the SGHF droplet gave much higher evaporation rates on its heated residue surface than on a heated copper surface. Following are the main conclusions from this study:

- The MR-2 SGHF exhibits the highest synergistic thermal conductivity among all experimentally studied mixing ratios.
- The low mixing ratio (MR $\leq$ 0.1) SGHF droplets give highest evaporation rates for substrate temperatures up to 100 °C.
- The high mixing ratio (MR $\geq$ 0.1) SGHF droplets give the highest evaporation rates in the nucleate boiling regime.
- The SGHF droplet evaporation rate on its residue surface increases up to 173% at T_s = 100 °C and by an order of magnitude in the nucleate boiling regime as compared to a copper surface.
- The SGHF droplet evaporation rate increases up to 218% with increasing droplet volume from 3 µl to 60 µl at a copper surface temperature of T_s =100 °C.
- At the critical point (C_p), the SGHF droplet evaporation rate increases up to 8 times with increasing droplet volume from 3 µl to 60 µl on a copper surface.
- A 3 µl MR-5 droplet exhibits the highest latent heat flux of 890 W/cm^2 and 850 W/cm^2 on heated copper and residue surfaces, respectively, at the critical point of $T_s \approx$ 125 °C.

Acknowledgements

The funding for this research is provided by the Hong Kong PhD Fellowship Scheme (HKPFS), the Hong Kong Research Grant Council via Collaborative Research Fund (CRF) account C6022-16G, General Research Fund (GRF) account 17205419 and Early Career Scheme (ECS) account 21200819.

References

[1] C.Y. Tso, C.Y.H. Chao, Study of enthalpy of evaporation, saturated vapor pressure and evaporation rate of aqueous nanofluids, Int. J. Heat Mass Transf. 84 (2015) 931–941. https://doi.org/10.1016/j.ijheatmasstransfer.2015.01.090.

[2] S. Fu, C. Tso, Y. Fong, C.Y.H. Chao, Evaporation of Al2O3-water nanofluids in an externally micro-grooved evaporator, Sci. Technol. Built Environ. 23 (2017) 345–354. https://doi.org/10.1080/23744731.2016.1250562.

[3] C.Y. Tso, S.C. Fu, C.Y.H. Chao, A semi-analytical model for the thermal conductivity of nanofluids and determination of the nanolayer thickness, Int. J. Heat Mass Transf. 70 (2014) 202–214. https://doi.org/https://doi.org/10.1016/j.ijheatmasstransfer.2013.10.077.

[4] D. Yoo, Thermal Conductivity of Al2O3/Water Nanofluids, J. Korean Phys. Soc. 51 (2007) 84–87.

[5] M. Chandrasekar, S. Suresh, A. Chandra Bose, Experimental investigations and theoretical determination of thermal conductivity and viscosity of Al2O3/water nanofluid, Exp. Therm. Fluid Sci. 34 (2010) 210–216. https://doi.org/https://doi.org/10.1016/j.expthermflusci.2009.10.022.

[6] W. Duangthongsuk, S. Wongwises, Measurement of temperature-dependent thermal conductivity and viscosity of TiO2-water nanofluids, Exp. Therm. Fluid Sci. 33 (2009) 706–714. https://doi.org/https://doi.org/10.1016/j.expthermflusci.2009.01.005.

[7] S.H. Kim, S.R. Choi, D. Kim, Thermal Conductivity of Metal-Oxide Nanofluids: Particle Size Dependence and Effect of Laser Irradiation, J. Heat Transfer. 129 (2006) 298–307. https://doi.org/10.1115/1.2427071.

[8] H.E. Patel, T. Sundararajan, S.K. Das, An experimental investigation into the thermal conductivity enhancement in oxide and metallic nanofluids, J. Nanoparticle Res. 12 (2010) 1015–1031. https://doi.org/10.1007/s11051-009-9658-2.

[9] L. Yang, J. Xu, K. Du, X. Zhang, Recent developments on viscosity and thermal conductivity of nanofluids, Powder Technol. 317 (2017) 348–369. https://doi.org/10.1016/j.powtec.2017.04.061.

[10] S. Akilu, K. V. Sharma, A.T. Baheta, R. Mamat, A review of thermophysical properties of water based composite nanofluids, Renew. Sustain. Energy Rev. 66 (2016) 654–678. https://doi.org/10.1016/j.rser.2016.08.036.

[11] W. Williams, J. Buongiorno, L.-W. Hu, Experimental Investigation of Turbulent Convective Heat Transfer and Pressure Loss of Alumina/Water and Zirconia/Water Nanoparticle Colloids (Nanofluids) in Horizontal Tubes, J. Heat Transfer. 130 (2008). https://doi.org/10.1115/1.2818775.

[12] C.T. Nguyen, F. Desgranges, G. Roy, N. Galanis, T. Maré, S. Boucher, H. Angue Mintsa, Temperature and particle-size dependent viscosity data for water-based nanofluids – Hysteresis phenomenon, Int. J. Heat Fluid Flow. 28 (2007) 1492–1506. https://doi.org/https://doi.org/10.1016/j.ijheatfluidflow.2007.02.004.

[13] S.K. Sharma, S.M. Gupta, Preparation and evaluation of stable nanofluids for heat transfer application: A review, Exp. Therm. Fluid Sci. 79 (2016) 202–212. https://doi.org/10.1016/j.expthermflusci.2016.06.029.

[14] E.B. Haghighi, N. Nikkam, M. Saleemi, M. Behi, S.A. Mirmohammadi, H. Poth, R. Khodabandeh, M.S. Toprak, M. Muhammed, B. Palm, Shelf stability of nanofluids and its effect on thermal conductivity and viscosity, Meas. Sci. Technol. 24 (2013) 105301. https://doi.org/10.1088/0957-0233/24/10/105301.

[15] M.J. Nine, H. Chung, M.R. Tanshen, N.A.B.A. Osman, H. Jeong, Is metal nanofluid reliable as heat carrier?, J. Hazard. Mater. 273 (2014) 183–191. https://doi.org/10.1016/j.jhazmat.2014.03.055.

[16] F.R. Siddiqui, C.Y. Tso, K.C. Chan, S.C. Fu, C.Y.H. Chao, On trade-off for dispersion

stability and thermal transport of Cu-Al2O3 hybrid nanofluid for various mixing ratios, Int. J. Heat Mass Transf. 132 (2019) 1200–1216. https://doi.org/https://doi.org/10.1016/j.ijheatmasstransfer.2018.12.094.

[17] F.R. Siddiqui, C.Y. Tso, S.C. Fu, H. Qiu, C.Y.H. Chao, Droplet Evaporation of Cu– Al2O3 Hybrid Nanofluid Over Its Residue and Copper Surfaces: Toward Developing a New Analytical Model, J. Heat Transfer. 143 (2021) 1–11. https://doi.org/10.1115/1.4048970.

[18] K.Y. Leong, K.Z. Ku Ahmad, H.C. Ong, M.J. Ghazali, A. Baharum, Synthesis and thermal conductivity characteristic of hybrid nanofluids – A review, Renew. Sustain. Energy Rev. 75 (2017) 868–878. https://doi.org/10.1016/j.rser.2016.11.068.

[19] J. Sarkar, P. Ghosh, A. Adil, A review on hybrid nanofluids: Recent research, development and applications, Renew. Sustain. Energy Rev. 43 (2015) 164–177. https://doi.org/https://doi.org/10.1016/j.rser.2014.11.023.

[20] J.A. Ranga Babu, K.K. Kumar, S. Srinivasa Rao, State-of-art review on hybrid nanofluids, Renew. Sustain. Energy Rev. 77 (2017) 551–565. https://doi.org/10.1016/j.rser.2017.04.040.

[21] M. Batmunkh, M.R. Tanshen, M.J. Nine, M. Myekhlai, H. Choi, H. Chung, Thermal Conductivity of TiO2 Nanoparticles Based Aqueous Nanofluids with an Addition of a Modified Silver Particle, Ind. Eng. Chem. Res. 53 (2014) 8445–8451. https://doi.org/10.1021/ie403712f.

[22] M.J. Nine, M. Batmunkh, J.H. Kim, H.S. Chung, H.M. Jeong, Investigation of Al2O3-MWCNTs Hybrid Dispersion in Water and Their Thermal Characterization, J. Nanosci. Nanotechnol. 12 (2012) 4553–4559. https://doi.org/10.1166/jnn.2012.6193.

[23] S. Suresh, K.P. Venkitaraj, P. Selvakumar, M. Chandrasekar, Synthesis of Al2O3–Cu/water hybrid nanofluids using two step method and its thermo physical properties, Colloids Surfaces A Physicochem. Eng. Asp. 388 (2011) 41–48. https://doi.org/https://doi.org/10.1016/j.colsurfa.2011.08.005.

[24] M.R. Han, Z. H, Yang, B., Kim, S. H., Zachariah, Application of hybrid sphere/carbonnanotube particles in nanofluids, Nanotechnology. 18 (2007) 105–109.

827 [25] M.U. Sajid, H.M. Ali, Thermal conductivity of hybrid nanofluids : A critical review, Int. J.
828 Heat Mass Transf. 126 (2018) 211–234.
829 https://doi.org/10.1016/j.ijheatmasstransfer.2018.05.021.

830 [26] N.A. Che Sidik, M. Mahmud Jamil, W.M.A. Aziz Japar, I. Muhammad Adamu, A review
831 on preparation methods, stability and applications of hybrid nanofluids, Renew. Sustain.
832 Energy Rev. (2017). https://doi.org/10.1016/j.rser.2017.05.221.

833 [27] F.R. Siddiqui, C.Y. Tso, S.C. Fu, C.Y.H. Chao, H.H. Qiu, Experimental Investigation On
834 Silver-Graphene Hybrid Nanofluid Droplet Evaporation And Wetting Characteristics Of Its
835 Nanostructured Droplet Residue, in: Proc. ASME-JSME-KSME 8th Jt. Fluids Eng. Conf.,
836 San Francisco, California, USA. July 28–August 1, 2019. Paper No: AJKFluids2019-5049,
837 V004T06A010, 2019. https://doi.org/https://doi.org/10.1115/AJKFluids2019-5049.

838 [28] K. Sefiane, R. Bennacer, Nanofluids droplets evaporation kinetics and wetting dynamics on
839 rough heated substrates, Adv. Colloid Interface Sci. 147–148 (2009) 263–271.
840 https://doi.org/https://doi.org/10.1016/j.cis.2008.09.011.

841 [29] Y.C. Kim, Evaporation of nanofluid droplet on heated surface, Adv. Mech. Eng. 7 (2015)
842 1–8. https://doi.org/10.1177/1687814015578358.

843 [30] A. Al-Sharafi, A.Z. Sahin, B.S. Yilbas, S.Z. Shuja, Marangoni convection flow and heat
844 transfer characteristics of water–CNT nanofluid droplets, Numer. Heat Transf. Part A Appl.
845 69 (2016) 763–780. https://doi.org/10.1080/10407782.2015.1090809.

846 [31] A. Al-Sharafi, H. Ali, B.S. Yilbas, A.Z. Sahin, M. Khaled, N. Al-Aqeeli, F. Al-Sulaiman,
847 Influence of thermalcapillary and buoyant forces on flow characteristics in a droplet on
848 hydrophobic surface, Int. J. Therm. Sci. 102 (2016) 239–253.
849 https://doi.org/https://doi.org/10.1016/j.ijthermalsci.2015.11.013.

850 [32] T. Okawa, K. Nagano, T. Hirano, Boiling heat transfer during single nanofluid drop impacts
851 onto a hot wall, Exp. Therm. Fluid Sci. 36 (2012) 78–85.
852 https://doi.org/https://doi.org/10.1016/j.expthermflusci.2011.08.007.

853 [33] G. Duursma, K. Sefiane, A. Kennedy, Experimental Studies of Nanofluid Droplets in Spray
854 Cooling, Heat Transf. Eng. 30 (2009) 1108–1120.

855 https://doi.org/10.1080/01457630902922467.

856 [34] G. Paul, P.K. Das, I. Manna, Nanoparticle deposition from nanofluid droplets during
857 Leidenfrost phenomenon and consequent rise in transition temperature, Int. J. Heat Mass
858 Transf. 148 (2020) 119110.
859 https://doi.org/https://doi.org/10.1016/j.ijheatmasstransfer.2019.119110.

860 [35] N.A.C. Sidik, I.M. Adamu, M.M. Jamil, G.H.R. Kefayati, R. Mamat, G. Najafi, Recent
861 progress on hybrid nanofluids in heat transfer applications: A comprehensive review, Int.
862 Commun. Heat Mass Transf. 78 (2016) 68–79.
863 https://doi.org/10.1016/j.icheatmasstransfer.2016.08.019.

864 [36] F.R. Siddiqui, C.Y. Tso, S.C. Fu, H.H. Qiu, C.Y.H. Chao, Evaporation and wetting behavior
865 of silver-graphene hybrid nanofluid droplet on its porous residue surface for various mixing
866 ratios, Int. J. Heat Mass Transf. 153 (2020) 119618.
867 https://doi.org/https://doi.org/10.1016/j.ijheatmasstransfer.2020.119618.

868 [37] P. Kelly-zion, C.J. Purcell, Evaporation of Sessile Drops under Combined Diffusion and
869 Natural Convection, Colloids Surfaces A Physicochem. Eng. Asp. 381 (2011) 31–36.

870 [38] F. Carle, B. Sobac, D. Brutin, Experimental evidence of the atmospheric convective
871 transport contribution to sessile droplet evaporation, Appl. Phys. Lett. 102 (2013) 061603.
872 https://doi.org/10.1063/1.4792058.

873 [39] D.P. Rini, R.-H. Chen, L.C. Chow, Bubble behavior and nucleate boiling heat transfer in
874 saturated FC-72 spray cooling, J. Heat Transfer. 124 (2002) 63–72.
875 https://doi.org/10.1115/1.1418365.

876 [40] R.-H. Chen, L.C. Chow, J.E. Navedo, Effects of spray characteristics on critical heat flux
877 in subcooled water spray cooling, Int. J. Heat Mass Transf. 45 (2002) 4033–4043.
878 https://doi.org/https://doi.org/10.1016/S0017-9310(02)00113-8.

879 [41] R.-H. Chen, D.S. Tan, K.-C. Lin, L.C. Chow, A.R. Griffin, D.P. Rini, Droplet and Bubble
880 Dynamics in Saturated FC-72 Spray Cooling on a Smooth Surface, J. Heat Transfer. 130
881 (2008). https://doi.org/10.1115/1.2953237.

882 [42] R.-H. Chen, L.C. Chow, J.E. Navedo, Optimal spray characteristics in water spray cooling,

883 Int. J. Heat Mass Transf. 47 (2004) 5095–5099.
884 https://doi.org/https://doi.org/10.1016/j.ijheatmasstransfer.2004.05.033.

885 [43] F.R. Siddiqui, C.Y. Tso, K.C. Chan, S.C. Fu, C.Y.H. Chao, Dataset on critical parameters
886 of dispersion stability of Cu/Al2O3 nanofluid and hybrid nanofluid for various ultra-
887 sonication times, Data Br. 22 (2019) 863–865.

888 [44] L. Karlsson, A. Ljung, T.S. Lundstrom, Comparing Internal Flow in Freezing and
889 Evaporating Water Droplets Using PIV, Water. 12 (2020) 1489.
890 https://doi.org/10.3390/w12051489.

891 [45] M. Mehrali, E. Sadeghinezhad, S.T. Latibari, S.N. Kazi, M. Mehrali, M.N.B.M. Zubir,
892 H.S.C. Metselaar, Investigation of thermal conductivity and rheological properties of
893 nanofluids containing graphene nanoplatelets, Nanoscale Res. Lett. 9 (2014) 15.
894 https://doi.org/10.1186/1556-276X-9-15.

895 [46] B. Takabi, S. Salehi, Augmentation of the heat transfer performance of a sinusoidal
896 corrugated enclosure by employing hybrid nanofluid, Adv. Mech. Eng. 6 (2014) 1–16.

897 [47] M. Bahiraei, Particle migration in nanofluids: A critical review, Int. J. Therm. Sci. 109
898 (2016) 90–113. https://doi.org/10.1016/j.ijthermalsci.2016.05.033.

899 [48] M. Bahiraei, S.M. Hosseinalipour, Particle migration in nanofluids considering
900 thermophoresis and its effect on convective heat transfer, Thermochim. Acta. 574 (2013)
901 47–54. https://doi.org/10.1016/j.tca.2013.09.010.

902

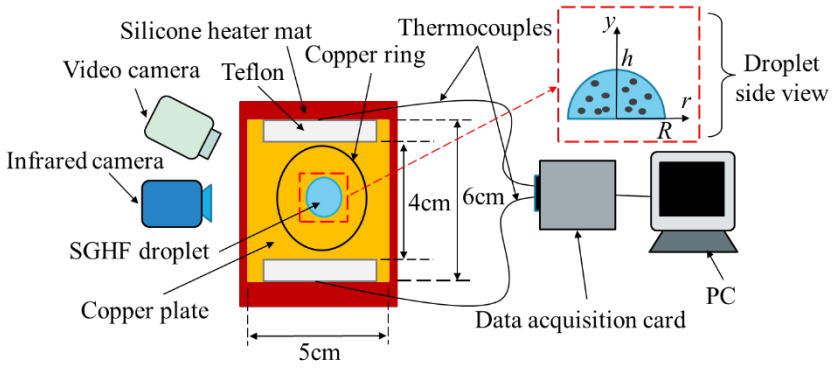

(a)

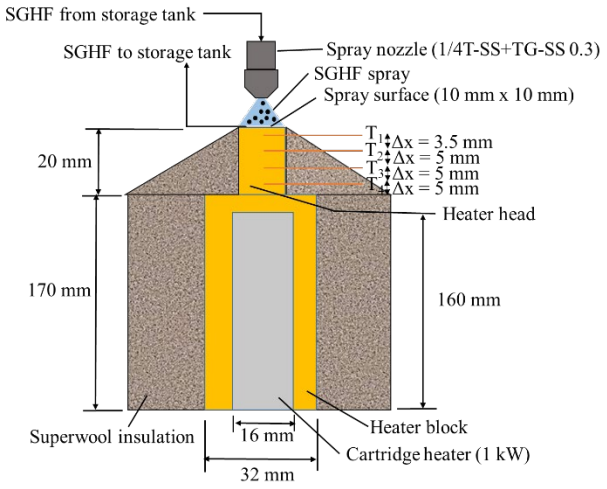

(b)

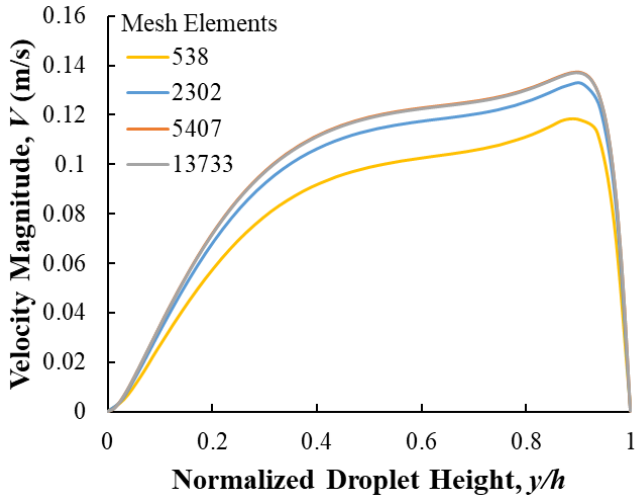

(c)

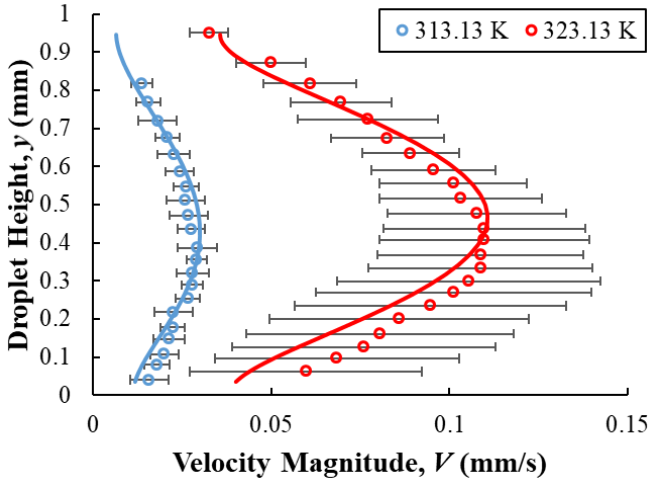

(d)

903 Fig. 1 (a) An experimental setup for the SGHF droplet evaporation and boiling investigation, (b) schematic of the SGHF spray cooling
904 setup, (c) mesh independence test for the SGHF droplet numerical modelling and (d) validation of our numerical model (solid lines)
905 using PIV experimental data (markers) [44].

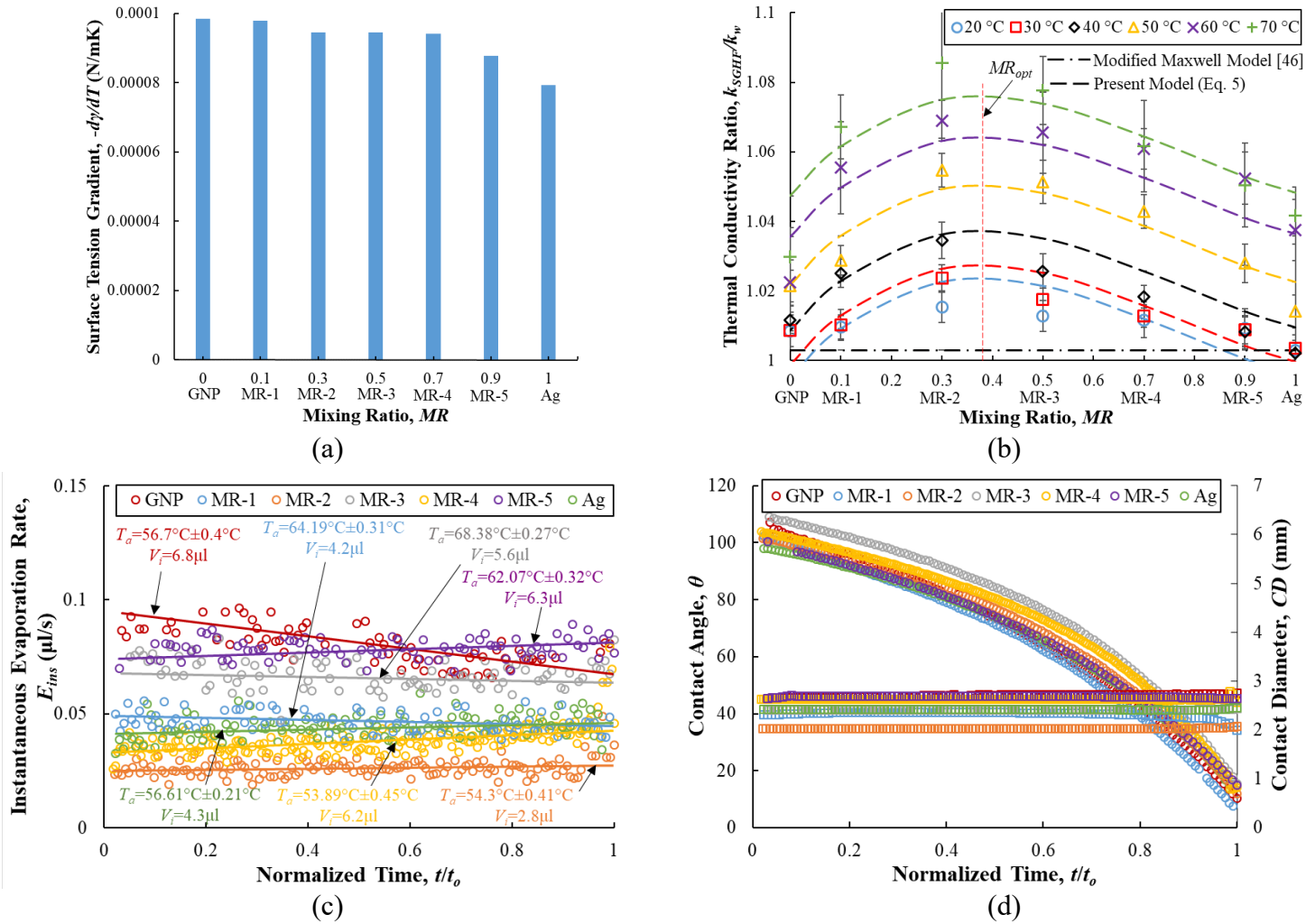

Fig. 2 (a) Surface tension gradient for different SGHF mixing ratios, (b) thermal conductivity ratio for SGHF mixing ratios at various temperatures, (c) droplet instantaneous evaporation rate, (d) contact angle and contact diameter during the droplet lifetime for various mixing ratios of the SGHF droplet on a heated copper substrate.

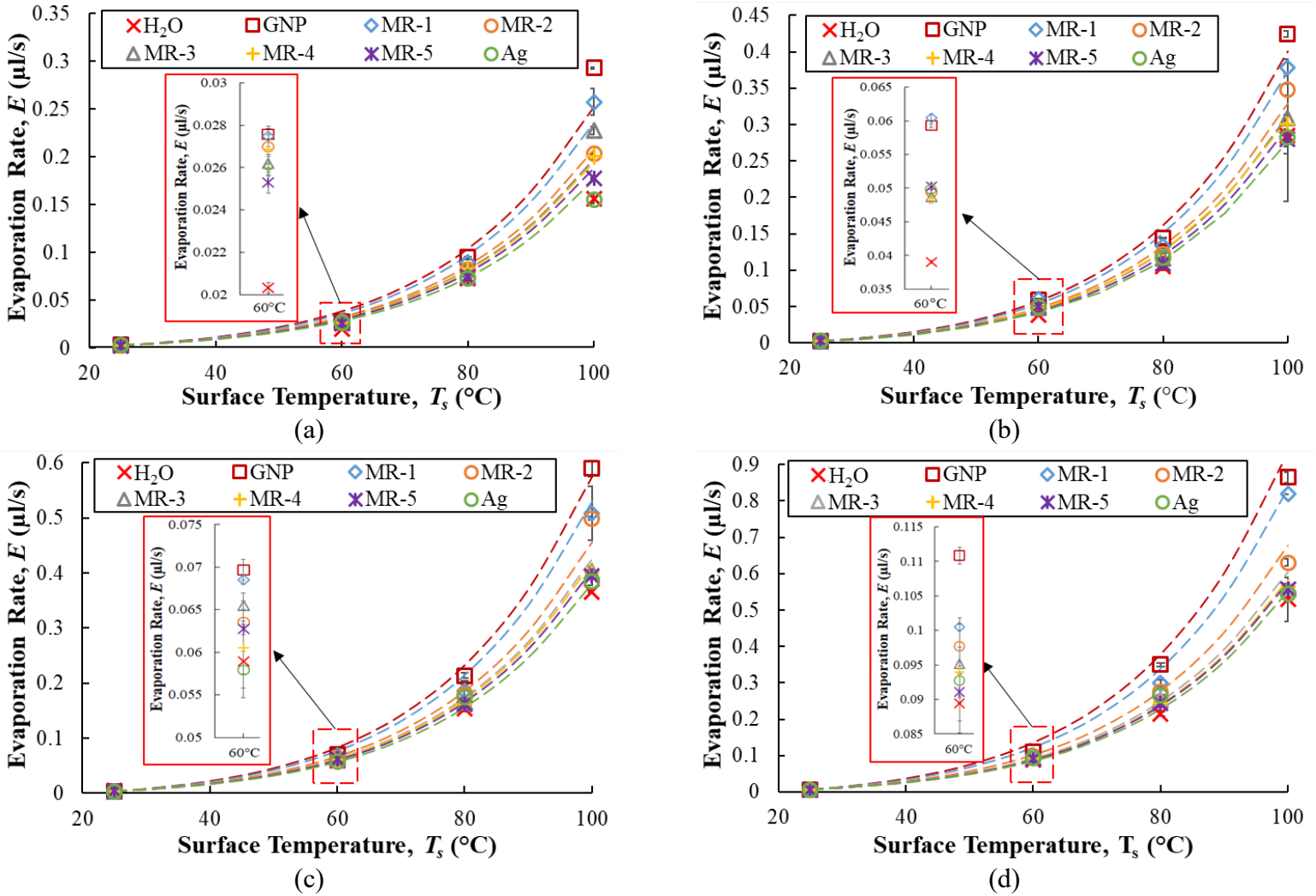

910 Fig. 3 Evaporation rate of different mixing ratios of SGHF droplets on a heated copper surface for droplet volume (V_{fd}) of (a) 3µl, (b)
911 15µl, (c) 30µl and (d) 60µl. Dashed lines are semi-empirical results (equation (14)) while colored markers correspond to experimental
912 results. Insets show enlarged plots for evaporation rate at surface temperature of 60 °C.

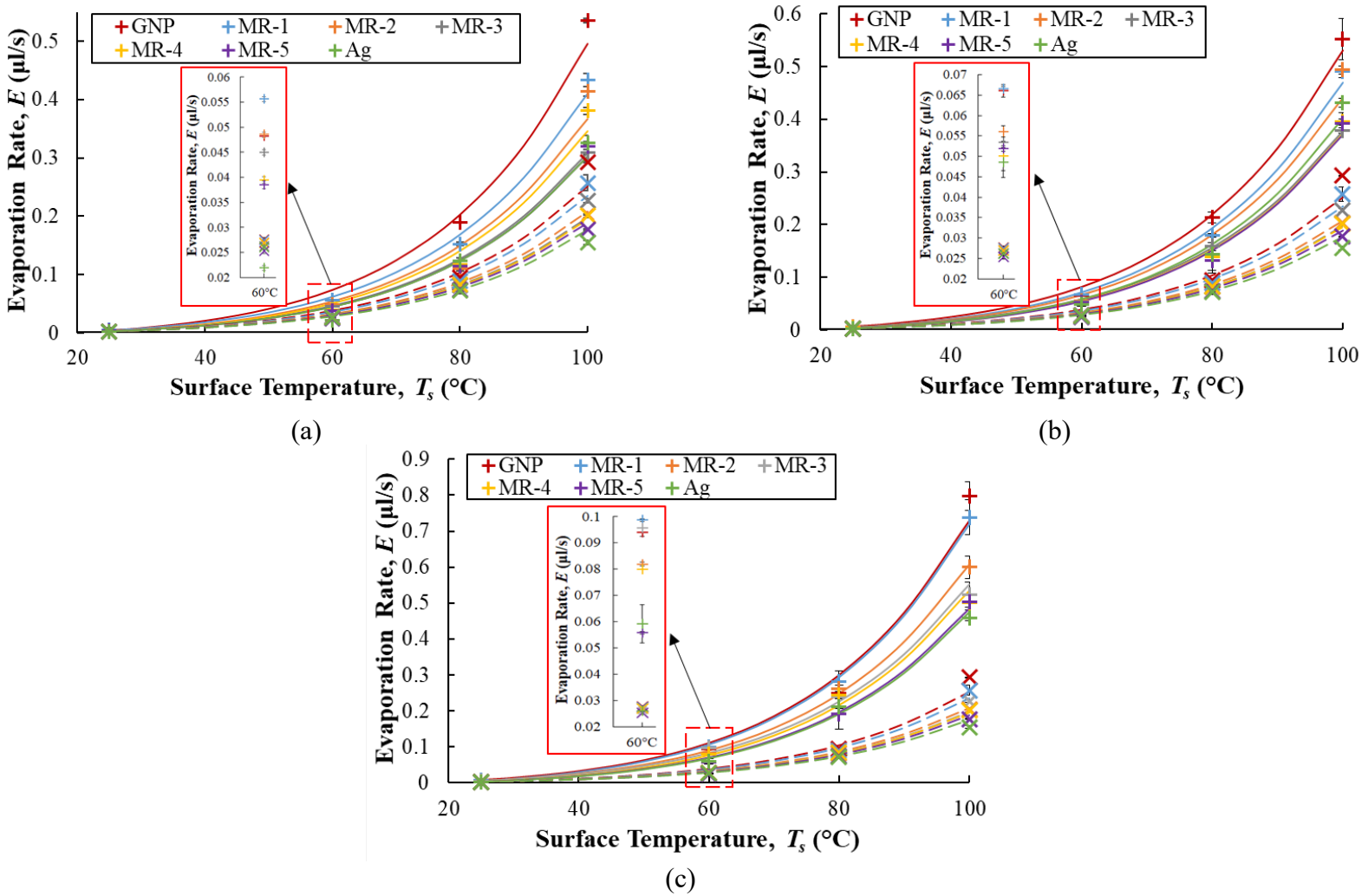

Fig. 4 Comparison of a 3µl SGHF droplet evaporation rate on heated copper (x markers) and residue (+ markers) surfaces for residue sizes of (a) $V_{fd}/V_{sd} = 5$, (b) $V_{fd}/V_{sd} = 10$ and (c) $V_{fd}/V_{sd} = 20$. Solid and dashed lines are semi-empirical results (equation (14)) for SGHF droplet evaporation rate on residue and copper surfaces, respectively. Insets show enlarged plots for evaporation rate at surface temperature of 60 °C.

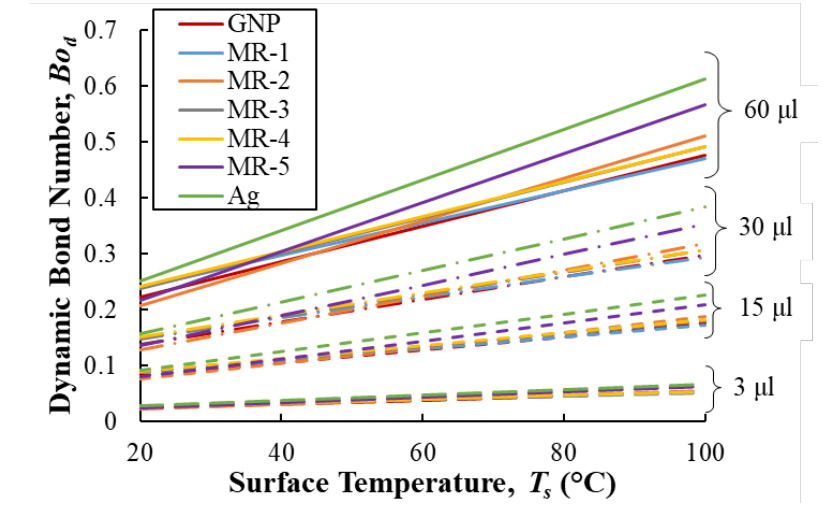

(a)

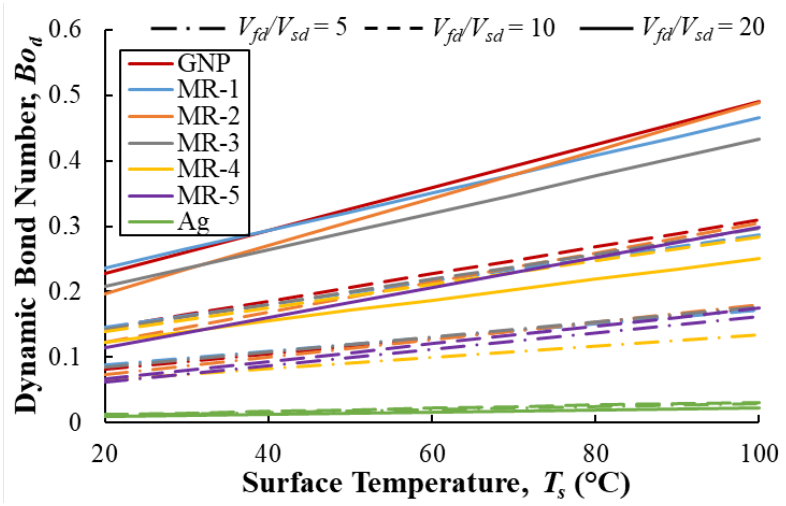

(b)

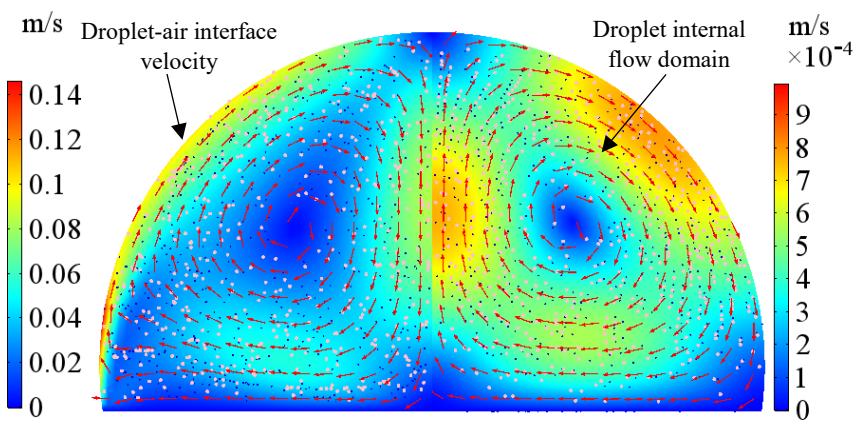

(c)

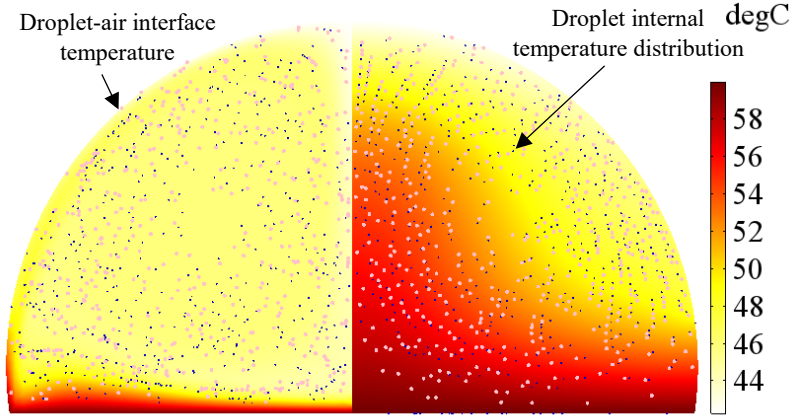

(d)

Fig. 5 Dynamic bond number for SGHF droplets of (a) V_{fd} = 3 µl, 15 µl, 30 µl, 60 µl on a copper surface and (b) V_{fd} / V_{sd} = 5, 10 and 20 on a residue surface, (c) Velocity profile and (d) temperature distribution inside a 15 µl SGHF (MR-3) droplet at start of evaporation (t = 2s) on a heated copper surface of temperature T_s = 60 °C. Droplet left half corresponds to combined thermal Marangoni and natural convection induced flow while droplet right half corresponds to only natural convection induced flow.

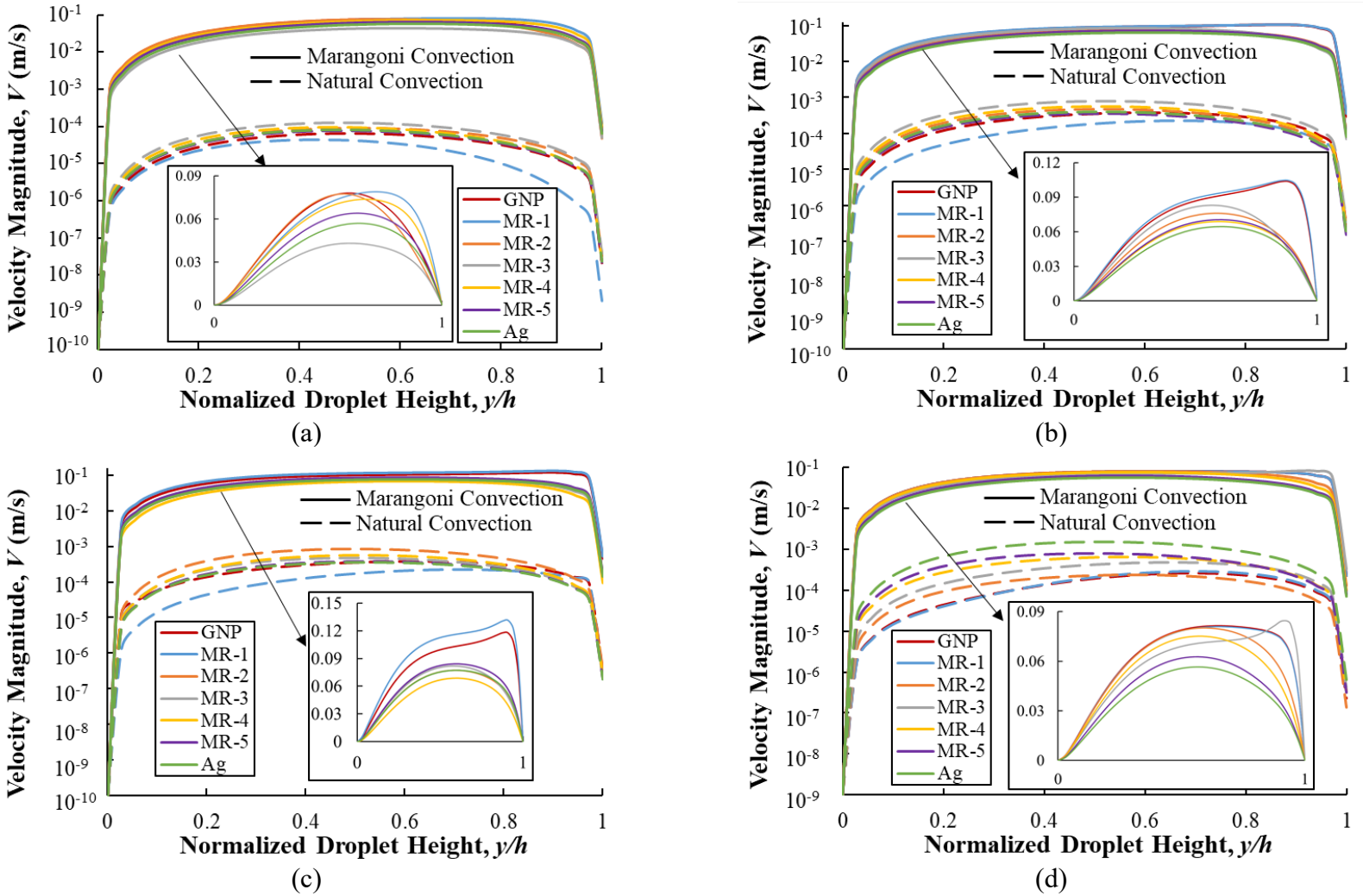

Fig. 6 Velocity magnitude along the droplet height (y/h) inside the SGHF droplet at start of evaporation (t = 2s) for droplet volume (V_{fd}) of (a) 3µl, (b) 15µl, (c) 30µl and (d) 60µl on a heated copper surface of 60 °C temperature. Insets show the Marangoni convection induced velocity magnitude plots on linear y-scale.

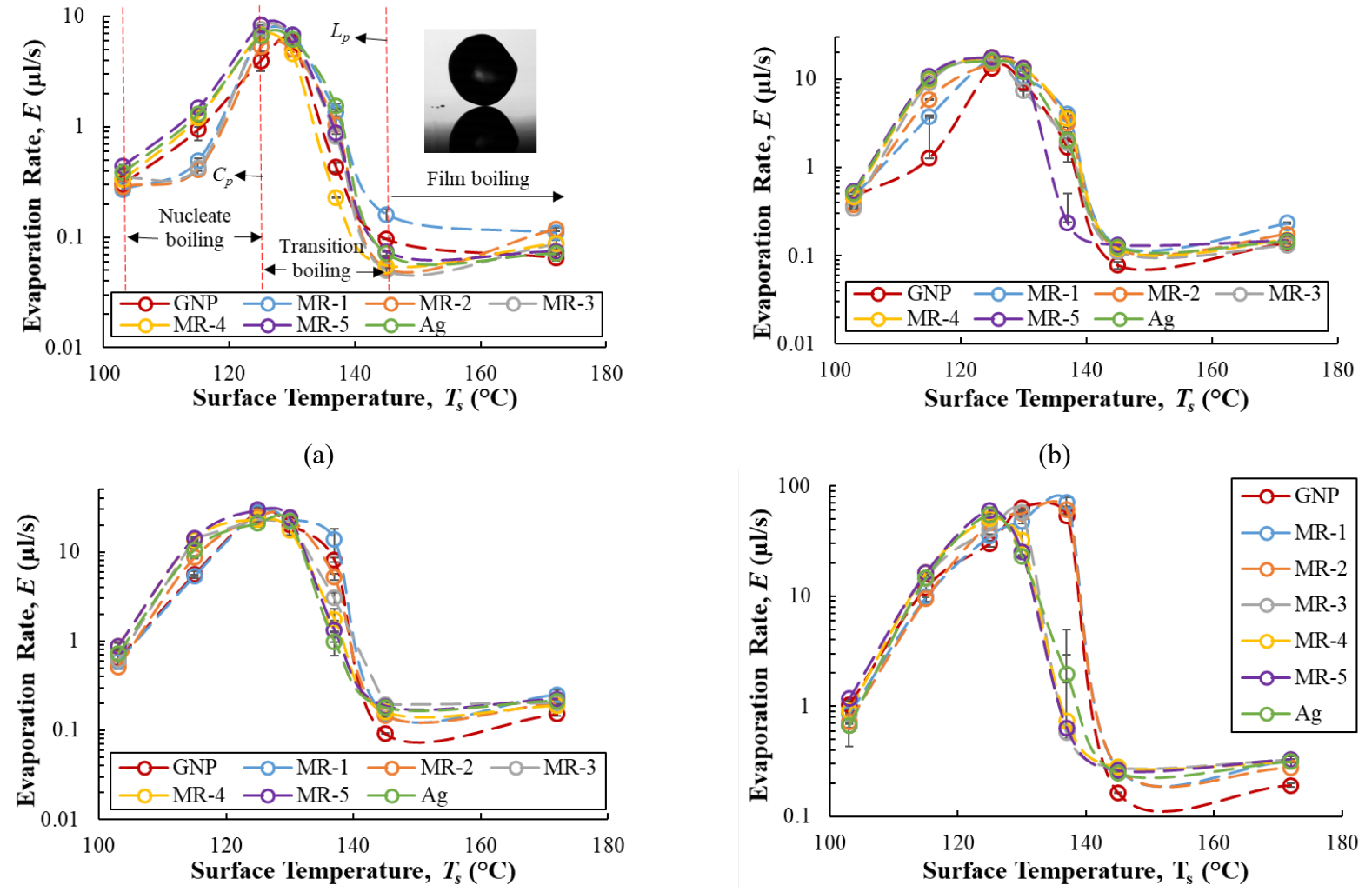

924 Fig. 7 Evaporation rate for various mixing ratios of SGHF droplets on a copper surface for droplet volume of (a) 3µl, (b) 15µl, (c) 30µl
925 and (d) 60µl in the boiling regime.

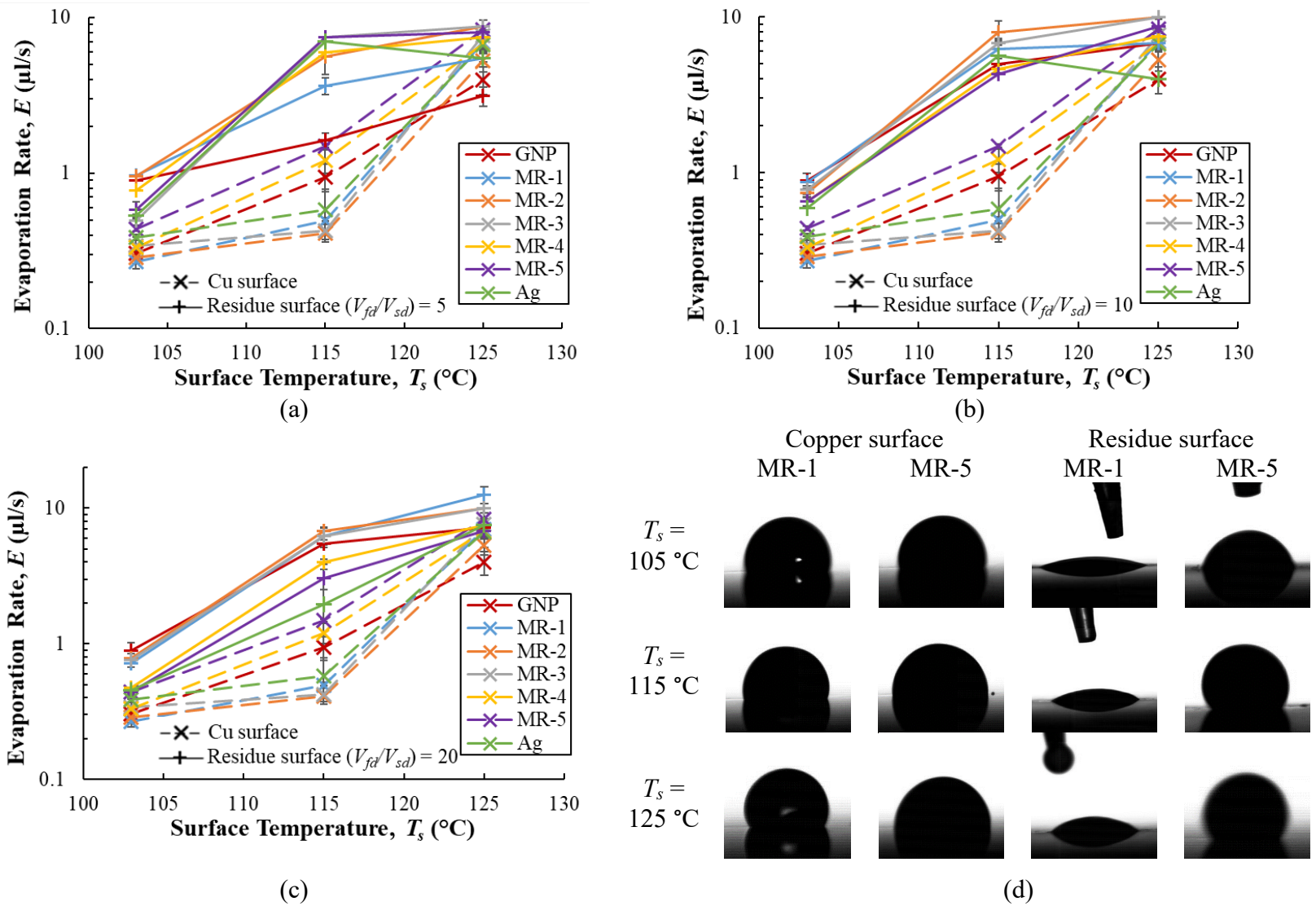

926 Fig. 8 Comparison in evaporation rate of a 3 µl SGHF droplet on a copper surface and residue surfaces for (a) $V_{fd}/V_{sd} = 5$, (b) $V_{fd}/V_{sd} =$
927 10 and (c) $V_{fd}/V_{sd} = 20$ in the nucleate boiling regime (103 °C ≤ T_s ≤ 125 °C), (d) comparison of surface wettability for low (MR-1)
928 and high (MR-5) mixing ratio droplets on heated copper and residue ($V_{fd}/V_{sd} = 20$) surfaces in the nucleate boiling regime.

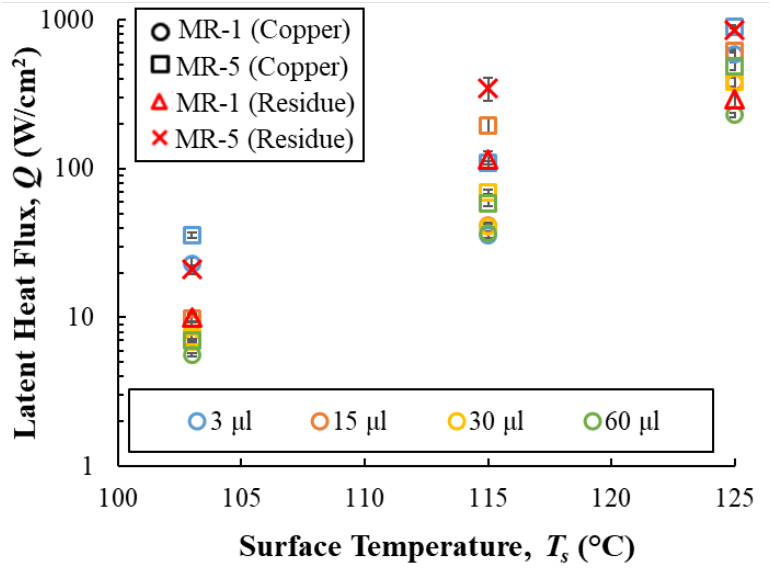

(a)

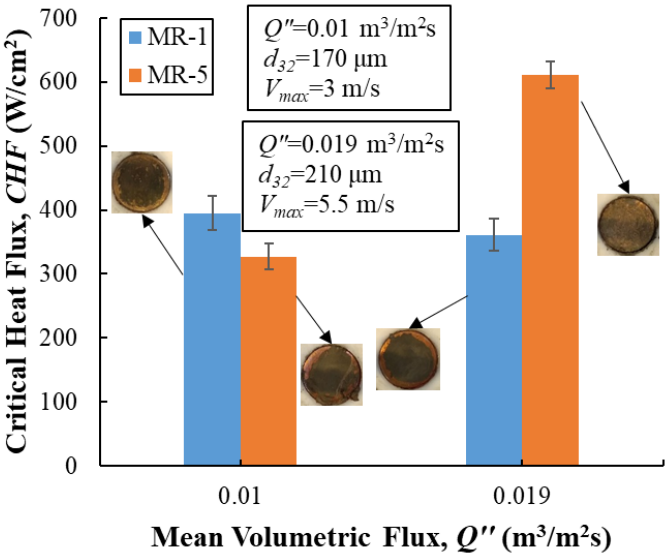

(b)

Fig. 9 (a) Latent heat flux for various droplet volumes of low mixing ratio (MR-1) and high mixing ratio (MR-5) SGHF droplets on copper and residue (V_{fd}/V_{sd} = 20) surfaces in the nucleate boiling regime, (b) effect of spray hydrodynamic parameters on critical heat flux (CHF) of MR-1 and MR-5 SGHF sprays. Insets show spray residues at the end of SGHF spray cooling process.